

Investigation and Development of MR-Compatible Actuation Methods for Multi-Axis Robots

Xue Yin Zhang

A thesis submitted in fulfilment
of the requirements of the degree of
Bachelor of Engineering (Mechatronic (Space))/Bachelor of Arts (Music)



Supervisor: André Kyme
Co-supervisor: Graham Brooker
School of Aerospace, Mechanical and Mechatronic Engineering
The University of Sydney

November 2018

Declaration

The work presented herein is substantially my own except for the contributions which is as follows:

- I conducted the literature survey that gives context to the work which has been carried out in this thesis project. At the start of this project, my supervisor provided me with a list of papers to guide my reading.
- I designed the model for the open loop ceramic motor jig with the help of Andrei Lozzi. The parts were then machined in the AMME workshop by Stanley Kakarda. I assembled the jig. I also wrote the program to control the motor with help from Brian Ki Myung Lee.
- André Kyme designed and constructed the closed loop ceramic motor jig from Lego with the (very helpful) assistance of his children.
- Full credit goes to Aidan McDaid from Boston University who designed, built, and tested the pneumatic rotary stepper motor during Semester 1 2018. McDaid also wrote the Arduino program to control the motor.
- I designed the CAD model for the pneumatic cylinder jig, fabricated its parts, and constructed the jig. I wrote the Arduino program to control the motor.
- I tested the above actuators at two MRI facilities with the help of Bin Dong, Sofie Trajanovska, Binh Pham, and Nana Sunn who operated the MRI scanners and conducted the scanning procedures. André Kyme assisted with the experimental setup and transport of equipment to and from our lab.
- I wrote the program to process the scan data on MATLAB with guidance from Bin Dong and Sofie Trajanovska on proper analytical procedure.

- I developed the pneumatic curvilinear stepper motor and designed the CAD models for it.
- I fabricated and constructed the acrylic curvilinear stepper motor prototypes.
- I fabricated and constructed the resin curvilinear stepper motor prototypes. Benjamin van Magill assisted with the first prototype, but fabrication of the subsequent prototype was carried out by myself.
- I wrote the Arduino program to control the pneumatic curvilinear stepper motor.
- I conducted experiments to measure load and bandwidth on the curvilinear motor, and was assisted by Graham Brooker and Mitch Bryson who provided advice on the testing procedure.

Signed:

Xue Yin Zhang(student)

Date:

André Kyme (supervisor)

Date:

Graham Brooker (co-supervisor)

Date:

Abstract

In magnetic resonance (MR)-guided radiotherapy systems, real-time scan images of the cancer patient is used to compensate for the patient's movements during the treatment. However, even recent systems such as magnetic resonance imaging(MRI)-linear accelerator(LINAC) face the challenge of the lack of a standard procedure for systematic quality assurance testing. In light of the recent successes of MR-compatible robotics in surgical applications, we propose to develop an MR-compatible robotic platform that can manipulate a phantom to generate a ground truth motion to benchmark motion-adaptive techniques in MR-guided radiotherapy. To do so, we first investigated different MR-compatible actuation methods including a ceramic motor, pneumatic stepper motor, air motor, and pneumatic cylinder. These methods were then implemented and evaluated in terms of the impact on signal-to-noise-ratio (SNR) of the MRI scan images, which is an indicator of MR-compatibility. It is found that for three different experimental settings, pneumatic actuation exhibits the least impact on SNR, and ceramic motors the worst. Based on this finding, we designed and fabricated a pneumatic curvilinear stepper motor, which exhibits up to 37 Hz stepping frequency and a maximum stall load of 1.6 N at 3 bar pressure. These characteristics indicate that the proposed pneumatic curvilinear stepper motor is can be developed into a phantom manipulator for benchmarking MR-guided radiotherapy systems.

Acknowledgements

I am indebted to a great many number of people who have each had a hand or a foot in pushing this thesis project forward. Deep gratitude and thanks go toward:

- **André Kyme** for sharing your intellect, knowledge, and spirit of dedication with me. Your unending support and guidance has been of immense help throughout the year.
- **Graham Brooker** for the indispensable advice you have offered along the way.
- **Gary Liney** for making this project possible.
- **Sofie Trajanovska, Binh Pham, Nana Sunn, and Bin Dong** for accommodating for our experiments with your time and resources.
- **Aidan McDaid** for your significant contribution to this project.
- **Andy Wan** for always being of assistance at the AMME Fabrication Lab whenever I asked for help.
- **Andrei Lozzi** for helping design the ceramic motor jig.
- **Ben van Magill** for teaching me how to use a resin printer.
- **Saree Analghy** for your expert advice and resources on motion-adaptive radiotherapy.
- **Brian Ki Myung Lee** for being a sounding board for all my ideas and challenges, and an all-round phenomenal person.
- **My immediate family** for your love and humour.

Why do scuba divers fall backwards off of the boat?

Because if they fell forward, they'd still be in the boat.

Contents

Declaration	i
Abstract	iii
Acknowledgements	v
Contents	vii
List of Figures	xi
List of Tables	xv
Acronyms	xvii
1 Introduction	1
1.1 Background and motivations	1
1.2 Project aim and scope	3
1.3 Organisation of the Thesis	4
2 Literature Review	5
2.1 Introduction	5
2.2 MR-compatible materials	6
2.3 Actuation, transmission, and control	6
2.3.1 Ceramic motors	7
2.3.2 Pneumatic actuation	8

2.3.3	Hydraulics	10
2.3.4	Mechanical transmission	10
2.4	Applications of magnetic resonance (MR)-compatible robots	11
2.4.1	Phantom manipulation	11
2.4.2	Stereotactic surgery	11
2.5	Summary	13
3	Methods	14
3.1	Actuator implementations	14
3.1.1	Ultrasonic motor design	15
3.1.2	Pneumatic actuator implementations	18
3.2	SNR Analysis	25
3.2.1	Testing signal-to-noise ratio (SNR) on the 7T small animal system .	26
3.2.2	Testing SNR on the 1.5T MRI-LINAC	30
3.3	Prototyping a pneumatic stepper motor	33
3.3.1	Proof of concept	35
3.3.2	Curvilinear stepper motor	35
3.3.3	Circular track	36
3.3.4	Mechanical stepping pattern	38
3.3.5	Fabrication	38
3.3.6	Pneumatic control	40
3.4	Actuator Characterisation	42
3.4.1	Load tests	44
3.4.2	Bandwidth tests	45
4	Results	47
4.1	Preliminary actuator implementation	47
4.1.1	Ceramic motor	47
4.1.2	Pneumatic actuators	47

4.2	SNR Analysis Results	48
4.2.1	7T small animal system	48
4.2.2	1.5T MRI-LINAC	51
4.3	Pneumatic motor prototyping	54
4.3.1	Proof of concept	54
4.3.2	Acrylic prototypes	55
4.4	Actuator Characterisation	57
4.4.1	Load tests	57
4.4.2	Bandwidth tests	58
5	Discussion	59
5.1	Preliminary actuator design	59
5.1.1	Ceramic motor	59
5.1.2	Pneumatic actuators	60
5.2	SNR Analysis	61
5.2.1	The poor MR-compatibility of ceramic motors	61
5.2.2	Choice of ROI	62
5.3	Prototyping	64
5.3.1	Air leakage	64
5.3.2	Friction and tolerancing	65
5.4	Actuator Characterisation	66
5.4.1	Load tests	66
5.4.2	Bandwidth tests	67
6	Conclusions	68
6.1	Summary	68
6.2	Findings and contributions	69
6.3	Future work	69
6.3.1	Refining the pneumatic curvilinear stepper motor	69
6.3.2	Simulation of a pneumatic Stewart platform	70
References		71

List of Figures

1.1	The 1.5T MRI-LINAC [1]	2
2.1	Ceramic motor with actuated parts labelled	7
2.2	Linear stepper motor by Secoli et al. [18]	9
2.3	Transperineal prostate needle placement [34]	12
3.1	Mechanical design for a ceramic motor actuator in open loop	15
3.2	Experimental setup for the open loop ceramic motor	16
3.3	Closing the loop for a ceramic motor system	17
3.4	Ceramic motor dataflow diagram - closed loop	17
3.5	Pneumatic system components	19
3.6	Switching the valves in the sequence 1-2-3-4 causes a clockwise rotation of the motor shaft	20
3.7	Pneumatic connections for the rotary stepper motor	20
3.8	Electrical connections for the rotary stepper motor	21
3.9	Deprag air motor	22
3.10	Pneumatic connections for the air motor	22
3.11	Electrical connections for the air motor	23
3.12	Double-acting cylinder	24
3.13	Pneumatic connections for the cylinder	24
3.14	States in the pneumatic cylinder system	24
3.15	Equipment setup during test scans	26
3.16	Phantom and scan slice setup	27

3.17 A ceramic motor is loaded at the edge of an RF coil, ready to be tested on the 7T scanner. Hidden from view is the falcon tube sitting in the middle of the RF coil.	27
3.18 Red = signal ROI, blue = background noise ROIs	29
3.19 An example of scans used for SNR calculation	32
3.20 Stepper motors designed by Groenhuis et al. [26]	33
3.21 Circular base Stewart platform [38]	34
3.22 A jig to demonstrate the stepping mechanism	35
3.23 Three different iterations of design for a curvilinear stepper motor	36
3.24 Circular track with sinusoidal teeth	37
3.25 Stepping mechanism of a pneumatic curvilinear stepper motor	38
3.26 Example of all the distinct layers required for the prototype in Figure 3.25b (relative sizes are not to scale)	39
3.27 Switching the valves in the sequence state 1-2-3-4 produced a counterclockwise movement of the motor relative to the circular track. Switching in the sequence state 4-3-2-1 produced a clockwise movement of the motor relative to the track.	40
3.28 Electrical connections for the four-chamber prototype actuator	41
3.29 Bench-top setup for load and bandwidth tests. A bag is tethered to the end of the pulley system to hold the weights.	42
3.30 Close up of the pulley system	43
4.1 SNR results from the 7T small animal system	49
4.2 Sample original scan images from the 7T small animal system	49
4.3 Sample scan images from the 7T small animal system with contrast adjusted to emphasise the image artefacts.	50
4.4 SNR results from the 1.5T MRI-LINAC (SE scans)	51
4.5 Sample scan images from the 1.5T MRI-LINAC (SE scans)	52
4.6 Sample scan images from the 1.5T MRI-LINAC with contrast adjusted to emphasise the image artefacts (SE scans)	53
4.7 SNR results from the 1.5T MRI-LINAC (HASTE scans)	53
4.8 Proof of concept for stepping mechanism	54

4.9	Pressurising chambers in the order 1-2-3-4 causes track to move to the right	55
4.10	Acrylic prototypes – four chamber, curvilinear track design	55
4.11	Resin prototypes – curvilinear track design	56
4.12	Experimental results for load capacity	57
4.13	Experimental results for bandwidth capacity	58
5.1	Contrast-adjusted scan image with ROI overlaid (7T small animal system) (red = signal ROI, blue = background ROI). Background ROI misses the ringing artefacts (left) but overlaps with the radiofrequency (RF) noise artefacts (right).	62
5.2	Vertical background ROIs for 7T small animal system data	63
5.3	Hypothetical SNR analysis results for vertical background ROIs for the 7T small animal system data	64
5.4	Most air leakage occurred at the sides of the acrylic curvilinear stepper motor	65
6.1	6-DOF Stewart platform with pneumatic curvilinear stepper motors as carriages	70

List of Tables

1.1	Desired specifications	4
3.1	Bill of equipment for the ceramic motor	18
3.2	Pneumatic system components	18
3.3	Bill of equipment or pneumatic actuators	19
3.4	Test configurations on the 7T small animal system	28
3.5	MRI scan parameters for our first test on the 7T small animal system . . .	28
3.6	MRI scan parameters for SE sequence on the 1.5T MRI-LINAC	30
3.7	MRI scan parameters for HASTE sequence on the 1.5T MRI-LINAC . . .	31
3.8	Test configurations on the 1.5T MRI-LINAC	31
3.9	Values for the standing wave parameters in the sinusoidal circular track. .	37
3.10	Activated outlet ports in each valve for each system state	41
3.11	Known masses in the pulley system	43
3.12	Experimental parameters for the load tests	45
3.13	Experimental parameters for the bandwidth tests	46

Acronyms

CAD	computer-aided design
CT	computed tomography
DOF	degree-of-freedom
EMI	electromagnetic interference
HASTE	half-Fourier acquisition single-shot turbo spin-echo
fMRI	functional magnetic resonance imaging
FOV	field of view
ID	inner-diameter
LINAC	linear accelerator
MR	magnetic resonance
MRI	magnetic resonance imaging
OD	outer diameter
PET	positron emission tomography
PLA	polylactic acid
RF	radiofrequency
ROI	region of interest
SE	spin echo
SNR	signal-to-noise ratio

Chapter 1

Introduction

1.1 Background and motivations

A common treatment offered to cancer patients is radiotherapy, which delivers a radiation beam at cancerous cells while sparing the surrounding normal tissue. A major challenge in radiotherapy is natural physiological movements, which cause tumours to deviate from radiation beam centre. Thus, the movements cause the treatment to be less effective, exposing the patient to unnecessary radiation dose.

A recently emerging solution to this problem is to employ a technique called motion-adaptive radiotherapy, where the patient is imaged at the same time as the radiotherapy treatment. The idea is that the motion-adaptive system can use the knowledge of a patient's real-time movements to compensate for the motion of a target tumour during the therapy.

A recent development in motion-adaptive radiotherapy in Australia that has gained a lot of research interest is a system called the MRI-LINAC, shown in Figure 1.1. The MRI-LINAC is the combination of an magnetic resonance imaging (MRI) scanner to provide the medical imaging and a linear accelerator (LINAC) to deliver the radiation treatment through a split in the bore of the MRI scanner.

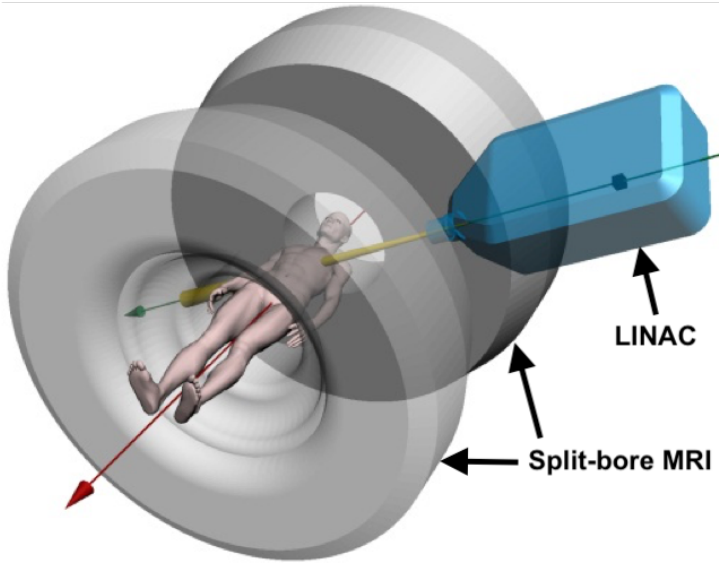


Figure 1.1: The 1.5T MRI-LINAC [1]

A challenge with the MRI-LINAC system is that there is – at present – no standard procedure for testing the performance of the system. Without quality assurance testing of the MRI-LINAC, there is no way of knowing whether the system is able to deliver radiotherapy treatment that is truly motion-adaptive. This is the main motivation of this thesis: we need a way of producing known, reproducible movements within the MRI-LINAC for quality assurance testing of the motion-adaptive radiotherapy system. Put another way, we need a robotic system that can be placed inside the MRI-LINAC to simulate natural physiological movements as a source of ground truth for quality assurance testing of the MR-guided radiotherapy system.

MRI scanners, however, are a notoriously difficult environment to operate in because of its extremely high magnetic field strength and switching magnetic field gradient during the scanning process. As is commonly known, any object made from ferromagnetic materials will be attracted to the scanner and become a projectile hazard, causing a lot of damage to the patient and the scanner if the object is untethered. Moreover, conventional electronic sensors and motors will behave unexpectedly under the strong magnetic field of an MRI scanner because of electromagnetic interference (EMI). Making a robotic system fully

MR-compatible is challenging because sophisticated conventional electronics can no longer be used within an MR environment.

In addition to the very high magnetic field strength, there is also the issue of accessibility to the machine. Space is already limited inside the bore of an MRI scanner with a patient in it, let alone is there much room left for a robotic system. If the robotic system relies on ferromagnetic devices to operate, these devices will have to be taken outside of the scan room, therefore necessitating long cables between the control devices outside the scan room and the robotic system inside.

One may argue that we can opt to use positron emission tomography (PET), computed tomography (CT) or X-ray scan to avoid this challenge. However, the pay-off for using MRI technology is that it offers excellent soft tissue contrast without using ionising radiation. By overcoming the hurdle of operating mechatronic systems within the harshness of an MR environment, novel MR-guided radiotherapy systems such as the MRI-LINAC have the potential to become a superior, minimally-invasive, form of treatment for cancer patients.

1.2 Project aim and scope

The aim of this thesis is to develop MR-compatible actuators that can be scaled into a multi-axis robotic platform for the purpose of quality assurance of MR-guided radiotherapy systems. This motivates the following tasks:

- Investigation of MR-compatible actuation methods,
- Design, fabrication, testing, and characterisation of prototype actuators,
- Design of a prototype robotic platform for possible future development.

The actuator must meet a number of criteria for a future application in a robotic platform. The criteria were identified as listed in Table 1.1.

Table 1.1: Desired specifications

Criteria	Value
Payload	1kg
Range of motion	$\pm 20^\circ$ rotations
Trajectory sampling rate	3.3 Hz

The payload criteria relates to the weight of an imaging phantom that the robotic platform must be able to support. The other criteria reflect the most extreme physiological movements present in a human body: lung expansion and contraction [2]. $\pm 20^\circ$ is the maximum range of motion that can be expected to occur, and 3.3 Hz is the minimum sampling rate required to reproduce a lung trace trajectory [2].

1.3 Organisation of the Thesis

This thesis is structured as follows:

Chapter 2 provides a literature review of the current work on MR-compatible robotic systems. The chapter discusses key past developments which influence and give context to the work that has been carried out in this thesis project.

Chapter 3 explains the methods that were used to design, build, and test a number of prototype MR-compatible actuators.

Chapter 4 lists the results that characterise our MR-compatible actuator over a number of key metrics for successful actuator design.

Chapter 5 contains a discussion and an in-depth analysis of the experimental results. It offers an interpretation of the data, and what it means for the viability of the MR-compatible actuator developed.

Chapter 6 summarises the main developments from this thesis project, and also suggests possible future work to extend what has been currently been achieved.

Chapter 2

Literature Review

2.1 Introduction

As an imaging modality, MRI technology has proven itself to be a highly advanced diagnostic tool that has been in widespread clinical use for a long time already. As mentioned earlier in the introduction, MRI technology has the benefit of producing high quality images without the ionising radiation exposure of other modalities like CT scans and X-ray imaging. Even when compared to ultrasound imaging, which does not use ionising radiation, MRI offers a higher contrast visualisation of soft tissues in both the target and surrounding area [3], making MRI a desirable instrument for precision applications.

Regarding the operating principles of an MRI scanner, the scanners use a very strong magnetic field – usually between 0.5-7T – to align the spin axes of the hydrogen protons in the patient’s body into a unidirectional magnetic vector [4]. The scanner then emits a high frequency RF pulse which causes the magnetic vector of hydrogen to relax, emit energy, and generate a signal which can be detected to form an MRI scan image [4]. By changing the gradient of the magnetic field, different slices of the body may be imaged. In short, MR-compatible components must be able to tolerate three hostile conditions: (1) very strong magnetic fields, (2) high frequency RF pulses, and (3) switching magnetic

field gradients [5].

2.2 MR-compatible materials

In this section, we present the background on MR-compatibility. For a piece of equipment to be considered MR-compatible, it must be made from non-ferromagnetic materials. If one was not careful and introduced a ferromagnetic component into the scanner, it could become a hazardous projectile due to the interaction between the magnetic field of the scanner and the ferromagnetic component. Not only must materials be non-ferromagnetic, but they must also be non-conductive. This is because the switching magnetic gradient of the scanner can induce eddy currents within the component and cause artefacts in the scan image [5]. Consequently, conductive but non-ferromagnetic objects are only permissible as long as they are small and securely fastened [3].

Ideal materials for MR-compatibility include plastics, ceramics, and composites which have been used in works such as [6–8]. Non-ferromagnetic metals like titanium, and zinc are also acceptable and commonly used [9, 10] because it is unlikely to suffer from eddy currents. Non-ferromagnetic metals that offer higher MR-compatibility include beryllium copper (CuBe), phosphorous copper (CuP), and brass [11]. When choosing materials for MR-compatible design, there is a trade-off between the stiffness and strength of metal, and the SNR passivity of plastics and ceramics.

2.3 Actuation, transmission, and control

In this section, we discuss previous work on actuation methods that fit within the constraint of MR-compatibility. A major challenge in MR-compatible robotics is in the limited selection of actuations methods available to work with. In a 2006 review of MR-compatible actuators, Gassert et al. [5] found that suitable actuation methods for MR

environments include pneumatics, hydraulics, electroactive polymers, cable/rod transmission, ultrasonic motors, and magnetomechanics, as these methods of actuation have evidence and precedence of success in the academic literature. In what follows, we discuss the relevant literature on these types of actuation methods.

2.3.1 Ceramic motors

A ceramic motor¹ exploits the piezoelectric effect of ceramics to generate motion. When a motor driver applies a high frequency, high voltage, and low current signal across a piece of ceramic, an ultrasonic vibration is induced in the ceramic motor tip [3]. The motor tip is loaded with a ceramic coupling, which is driven by the ultrasonic vibration. When the motor tip is coupled with a ceramic strip and linear slide, the vibrations will translate into linear motion of the strip. On the other hand, if the motor is coupled with a ceramic ring and bearing, the vibrations will translate into rotary motion, for example in Figure 2.1.

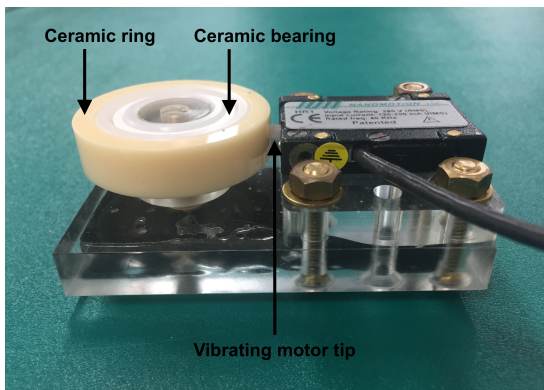


Figure 2.1: Ceramic motor with actuated parts labelled

Benefits of a ceramic motor include their compact size, nanoscale precision control, high bandwidth of at least 50Hz [5], and non-backdrivability. Although non-backdrivability would actually be a detriment to some robotic applications where human interaction is

¹Ceramic motors are also interchangeably called piezoelectric motors or ultrasonic motors

desired, it would actually be advantageous in our application as a MR-guided radiotherapy benchmarking tool where a robotic manipulator has to consistently drive a heavy payload.

There are, however, many drawbacks to ceramic motors. The biggest flaw reported in previous work is the moderate-to-severe drop in image SNR when the motor is in motion at the same time as the MRI scanning process [7, 12–14]. To mitigate this problem, some robotic systems based on ceramic motors were designed to be placed further away from the isocentre of the scanner [9], with others even requiring extra transmission to deliver actuation from outside the scanner into the destination within the scanner [10].

Many of the earliest seminal works in the field of MR-compatible robotics have used ceramic motors as their principal actuation method in their designs [10, 15, 16]. In more recent developments, authors have devised systems that interleave scanning and motor operation [3, 14]. However, switching off the motor is not feasible for our application where the robotic system is meant to be moving during the scan.

In summary, ceramic motors have both desirable qualities – compact and precise – and undesirable qualities – poor SNR performance – that demand further investigation. We are thus interested in conducting research on ceramic motors.

2.3.2 Pneumatic actuation

Many literature reviews agree that pneumatic tubes are the best option for maintaining a high SNR [3, 5, 12]. In addition to high SNR performance, pneumatically actuated systems are easily transportable to MRI scanner rooms as hospitals would normally have pneumatic compressors and supplies readily available. Pneumatics also provide reduced mechanical complexity as they do not require a return path for any exhaust air and or other air leakage [5]. On the downside, pneumatic actuation has a relatively low bandwidth, ranging up to 10Hz for shorter tube transmission, and a time delay between the compressor and the actuator due to the compressibility of air [3]. The compressibility

of air also causes low stiffness in the robotic joints, making it suitable only for smaller loads.

Typically, it is difficult to use pneumatics for continuous servo-control of a joint because of the following characteristics of air [6, 17]:

- Slow travel and response time, especially in long pneumatic lines (low bandwidth)
- Non-linearities in pneumatic lines and actuators due to the compressibility of air (complicated control problem to solve)

In 2007, Stoianovici et al. presented a pneumatic stepper motor called ‘PneuStep’ [6] which operates by sequentially pressurising three inlet ports to the motor. The sequential pressurisation of ports creates a switching signal in the pneumatic line and that can be approximated as discrete rather than continuous. In another example of discrete pneumatic control, Secoli et al. [18] produced a linear stepper motor using a simple guiding principle: pneumatic pistons can be modelled as a binary actuator by only considering the two end states of the piston. By coupling together multiple pistons for the actuation of one joint, pneumatic motors were able to produce discrete steps rather than a continuous movement as was previously the norm. The top-right of Figure 2.2 shows Secoli et al.’s 3-piston stepper motor. The bottom left object is an MR-compatible encoder.

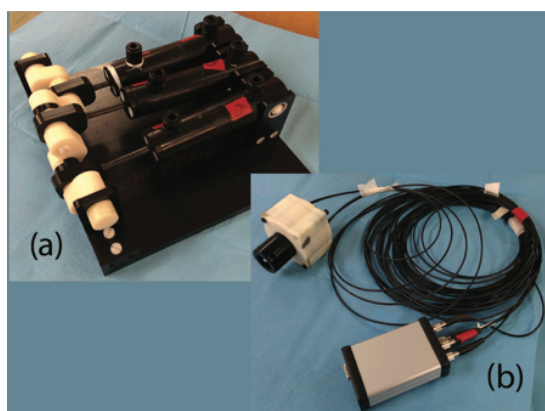


Figure 2.2: Linear stepper motor by Secoli et al. [18]

Following these seminal works on pneumatic stepper motors, research interest began to shift very quickly toward further improvements of pneumatic designs. The focus shifted from better control of a continuous pneumatic servo motor [17], to achieving better resolution with a discrete pneumatic stepper motor through coupling [18–21]. To this end, [21] achieved position control precision at the level of tens of microns.

As well as ceramic motors, pneumatic stepper motors are of interest to this project due to desirable traits like adequate open-loop performance and superior SNR performance. Pneumatic stepper motors are interesting because of their excellent SNR performance both when stationary and in motion [12], contrary to ceramic motors.

2.3.3 Hydraulics

Although pneumatics may seem to be a strong front-runner for MR-compatible actuation due to the high volume of research attention devoted to them, hydraulics is recently being developed, tested and validated. Hydraulic actuators are gaining substantial interest in the research community, including a best paper award at this year’s International Conference on Robotics and Automation (ICRA) [8].

Hydraulics have the advantage of high hose flexibility, and does not have problems associated with compressibility, with up to 20Hz bandwidth for shorter transmission lengths [5]. However, hydraulic systems can also be problematic due to high joint friction [5] and the safety hazards of fluid leakage or the introduction of air bubbles in the pressure system [3]. Hydraulics were ruled out for this project due to the dangers of improper hydraulics maintenance and the need for specialised knowledge and training in the area.

2.3.4 Mechanical transmission

Cables, shafts, and rods have been used successfully in the past [3, 5], but the need for fixed infrastructure make mechanical transmission too cumbersome and impractical for a

clinical MRI setting. Although tele-operated robotic systems are also available [22, 23], they are unsuitable for our purposes as they do not meet the reproducibility criterion.

2.4 Applications of MR-compatible robots

Recent advancements in MRI technology and increasing research interest in the imaging modality has created a demand for the use of robotic systems inside the MRI scanner. In the current state of the art, researchers have been developing robotic systems for highly specialised applications like stereotactic surgery and rehabilitation therapy during functional magnetic resonance imaging (fMRI).

2.4.1 Phantom manipulation

To the best of our knowledge, there is very sparse evidence of previous works in MR-compatible robotic platforms for the purposes of benchmarking MR-guided radiotherapy systems. The few examples of previous work that attempted to achieve MR-compatible, accurate, and reproducible motion of a phantom utilised single degree-of-freedom (DOF) [24, 25]. An obvious limitation is that there are not enough degrees of freedom in the device to represent natural physiological movements. Despite the lack of research in phantom manipulators application, there is still a wealth of knowledge about applications of MR-compatible robotics in medical procedures. In what follows, we discuss the wide body of literature on MR-compatible robotics for medical procedures to gain insights that are transferrable to the benchmarking problem.

2.4.2 Stereotactic surgery

Stereotactic surgery is the process of using a 3D coordinate system to perform medical procedures that require high-precision control. Medical imaging techniques like MRI can

be a useful tool for localising both the medical instrument and the target tissue in the patient to guide the stereotactic surgery procedure.

Ever since Masamune et al.'s [16] pioneering work on a 6-DOF MR-compatible needle insertion manipulator in 1995, robotics researchers have had a growing interest in using MR-compatible robotics for procedures like breast biopsy [22, 26], prostate biopsy [27–31], brachytherapy [20, 29, 32], and neurosurgery [8, 9]. These researchers have successfully implemented high DOF robotic system employing a range of actuation methods, including pneumatics [26, 28, 32], ceramic motors [9, 27] and even hydraulics [8].

General-purpose robotic systems for MR-guided stereotactic surgery have also been reported before [15, 31, 33], though they tend to be few and far between, and most other robotic systems target a particular task like prostate biopsy or brachytherapy. General-purpose robotic system often take the form of a multi-DOF robot arm that can be tele-operated [31, 33]. This type of design would be inappropriate for our purposes as they have been designed with the intent of manipulating a much lighter load of medical instruments. Driving a 1kg phantom payload would apply a high torque load on each individual joint in the arm, thus making a robotic arm design inappropriate for an MRI-LINAC benchmarking tool.

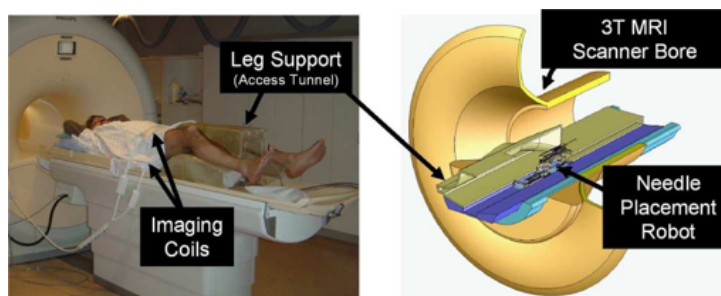


Figure 2.3: Transperineal prostate needle placement [34]

Prostate procedures specifically grew in popularity owing to the fact that typical MRI bores have limited space – around 60cm in diameter [22] –, and the best place to fit a sizeable robot is between the legs of the patient straddling the robot [27, 34] as shown in

Figure 2.3, or, alternatively with the patient lying on their side with their hips and knees at 90° as if sitting on the robot [28]. This way, the robot only the needle tip will intersect with the imaging slice during insertion, thus allowing for greater flexibility in choice of materials that might cause SNR losses but are more robust.

With needle insertion applications like biopsy, the highest priority for performance is position accuracy of the end effector, which is typically a sheath or tube with a needle inside. Even with Masanume et al's [16] early needle insertion manipulator, the team was able to achieve at worst 3mm accuracy with image feedback from an MRI scanner. While precision is certainly desirable for our applications, the challenge would be to adapt these robotics systems design for inserting medical devices into a system that can manipulate a heavy phantom payload.

2.5 Summary

Based on our survey of the field, it is evident that there is a limited extent of work on the use of MR-compatible robotics for phantom manipulation, as current research interest is primarily focussed on medical procedures. It is also evident that the rapid development of ceramic motor systems and the pneumatic stepper motor in stereotactic surgery applications show promising results in terms of precision and DOF, desirable qualities for phantom manipulation for quality assurance of MRI-LINAC. We are thus motivated to investigate the viability and efficacy of using ceramic and pneumatic motors.

Chapter 3

Methods

In this chapter, we describe the process of developing an MR-compatible actuator for benchmarking MR-guided radiotherapy. This process consisted of four stages of work. First, we implemented four existing MR-compatible actuators. We then tested these actuators at two MRI facilities to determine their impact on imaging SNR. Based on the SNR analysis results, we designed and fabricated several prototypes of a pneumatic curvilinear stepper motor that is suitable for a novel Stewart platform design. Finally, we tested the best prototype curvilinear stepper motor and characterised its performance.

3.1 Actuator implementations

In this section, we evaluate a series of actuators in order to understand the range of MR-compatible actuation methods available at our disposal. By testing and comparing the different types of actuators, we can make an assessment of their viability for a larger scale, multi-DOF robotic system with regard to the actuator's practicality and its SNR performance in an MRI environment. Specifically, we have tested an ultrasonic motor and three other actuators driven by pneumatics: a rotary stepper motor, air motor, and cylinder.

3.1.1 Ultrasonic motor design

This section details the implementation of a Nanomotion HR1 motor. Unlike conventional ‘plug-and-play’ motors, the Nanomotion HR1 motor requires a number of supporting hardware to control and drive the motor. The motor also has strict mechanical pre-loading requirements before the motor can be operated.

Mechanical design

The Nanomotion HR1 motor must be mounted and preloaded against the surface it is trying to drive before the motor can be operated [35]. To meet the precise preloading requirement, the motor was mounted on a jig, pressed up against a ceramic ring so that the motor tip was depressed by 1.2 mm, and then tightened into place.

The mechanical design for the open-loop ceramic motor is shown in Figure 3.1. In Figure 3.1b, the black box on the left side of the image is the actual motor itself. The acrylic jig was fabricated in-house at the AMME workshop and the ceramic ring and ceramic bearing were assembled. Figure 3.1a is a render of the CAD model designed to meet the strict preloading distance requirement of the motor tip.

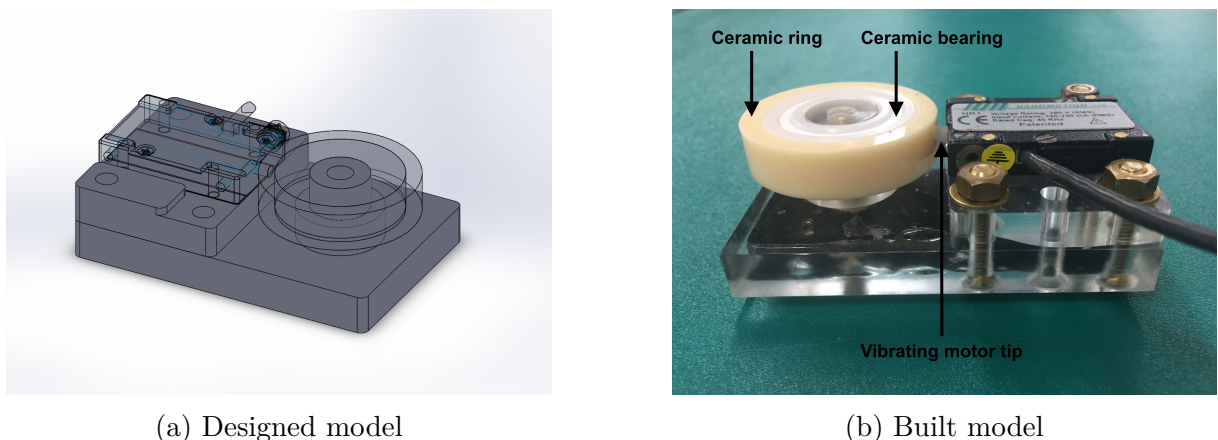


Figure 3.1: Mechanical design for a ceramic motor actuator in open loop

Hardware architecture

The hardware architecture for the open-loop system is shown in Figure 3.2. In the open loop system, the control chain began with the programmable motor controller. The motor controller sent a motor command signal to the motor driver, which converted the motor command into a high-voltage, high-frequency signal that induced vibrations in the ceramic motor tip. The motor controller in Figure 3.2 is in red to indicate that we programmed it. The ceramic motor is also in red to indicate that we designed and constructed the jig to support the ceramic motor.

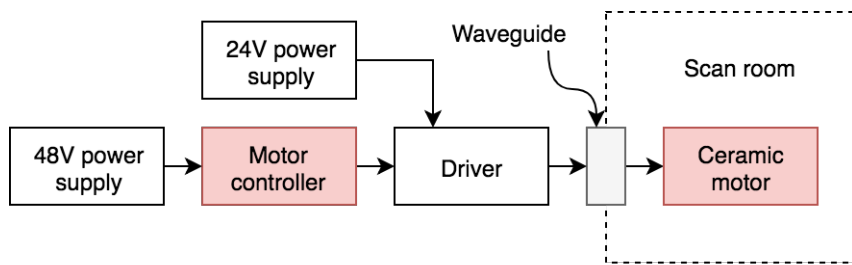


Figure 3.2: Experimental setup for the open loop ceramic motor

Closing the loop

To achieve an improved control of the ceramic motor, we implemented a closed-loop controller. The ceramic motor posed an interesting challenge when it came to closing the loop and providing feedback to a motor control system because any kind of feedback sensor had to be MR-compatible. Also, the ceramic motor did not have a natural position where an encoder could be easily mounted.

The experimental set-up for the closed-loop ceramic motor is shown in Figure 3.3. In a closed loop system, a ceramic bearing was coupled with a small rubber wheel. The rubber wheel drove a linear slide, which provided the compressive force to couple the rubber wheel to the ceramic bearing. An MR-compatible optical encoder was then coupled to the rubber wheel via a rubber tube – not visible in Figure 3.3 – which lessened the load on the encoder coupling shaft.

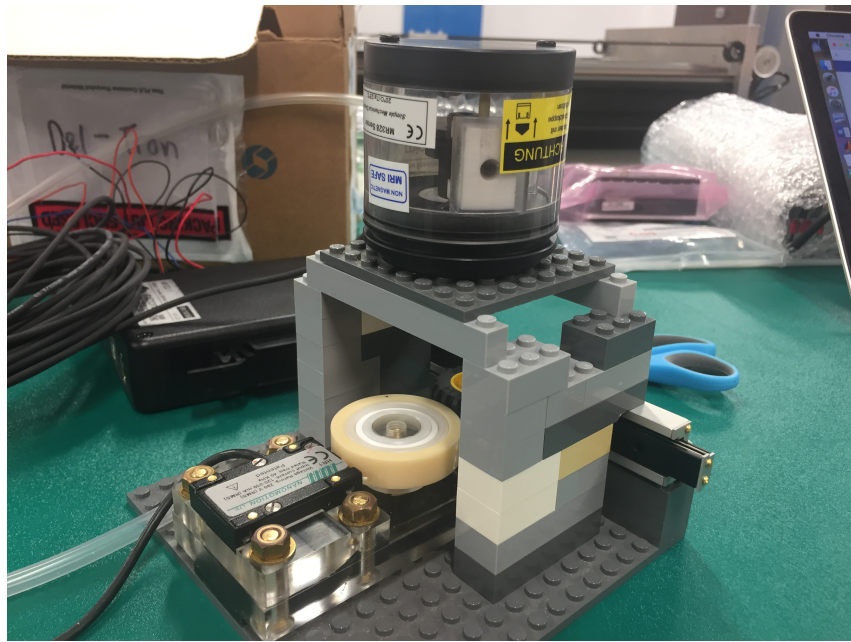


Figure 3.3: Closing the loop for a ceramic motor system

The dataflow diagram for the closed-loop system is shown in Figure 3.4. In addition to the open loop hardware architecture described in Section 3.1.1, the closed loop system had an additional optical encoder which was linked via fibre optic cable to an encoder controller (Figure 3.4). The encoder controller sent a quadrature signal back to the motor controller as feedback. A bill of equipment for the closed loop system is listed in Table 3.1.

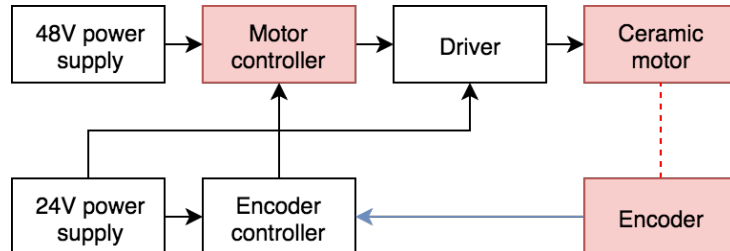


Figure 3.4: Ceramic motor dataflow diagram - closed loop

Table 3.1: Bill of equipment for the ceramic motor

Component	Manufacturer	Model
48V power supply	Galil	PSR-6-48
24V power supply	Unknown	Unknown
Controller	Galil	DMC-30012-BOX
Driver	Nanomotion	AB5-HR-E1
Optical encoder	Micronor	MR328
Encoder controller	Micronor	MR302-1

3.1.2 Pneumatic actuator implementations

The second actuation method we have tested is pneumatics. Unlike the ceramic motor, pneumatically driven actuators can have a number of different principles of actuation, a few of which have been tested by us. Diverse as they are, most pneumatic actuation systems require the same basic components, including a compressor, valves, a controller and pneumatic tubes. A functional description of these components is summarised in Table 3.2. The components used in this work are shown in Figure 3.5, and a bill of equipment is presented in Table 3.3.

Table 3.2: Pneumatic system components

Component	Purpose
Compressor	Stores and supplies compressed air to the rest of the system
Valves	Directs compressed air from the inlet into the desired outlet
Controller	Controls and switches the valves
Pneumatic tubes	Transport compressed air to the actuator

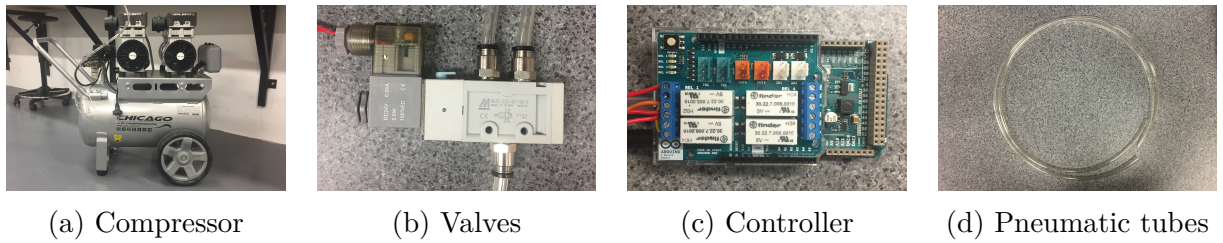


Figure 3.5: Pneumatic system components

Some pneumatic actuators have a continuous range of motion and require continuous control over air pressure to produce varying speeds. Other actuators have a discrete range of motion and rely on a fixed air pressure and switching valves to produce stepped motion. Different actuators require us to connect these components up into different configurations.

Table 3.3: Bill of equipment or pneumatic actuators

Model	Details
Chicago HUSH 50 Air Compressor	Fitted with a water filter and line pressure gauge
Mindman 5/2 Valves	Five port, two state valve with: <ul style="list-style-type: none"> • 1 inlet port • 2 outlet ports • 2 exhaust ports
Arduino Due	Mounted with an Arduino 4 Relays Shield
Pneumatic tubes	Two sizes used: <ul style="list-style-type: none"> • 5mm inner-diameter (ID), 8mm outer diameter (OD) • 4mm ID, 8mm OD

Rotary stepper motor

Aidan McDaid¹ designed and built a rotary stepper motor based on Groenhuis' work [36]. This stepper motor was modelled after the Bourke engine and has four pistons and four chambers. Our model is composed of 3D-printed polylactic acid (PLA) parts which were held together by nylon screws. Rubber sheets and silicone were used to minimise air leakage out of the piston chambers. As shown in Figure 3.6, the motor rotates in 90° increments by sequentially pressurising orthogonal chambers.

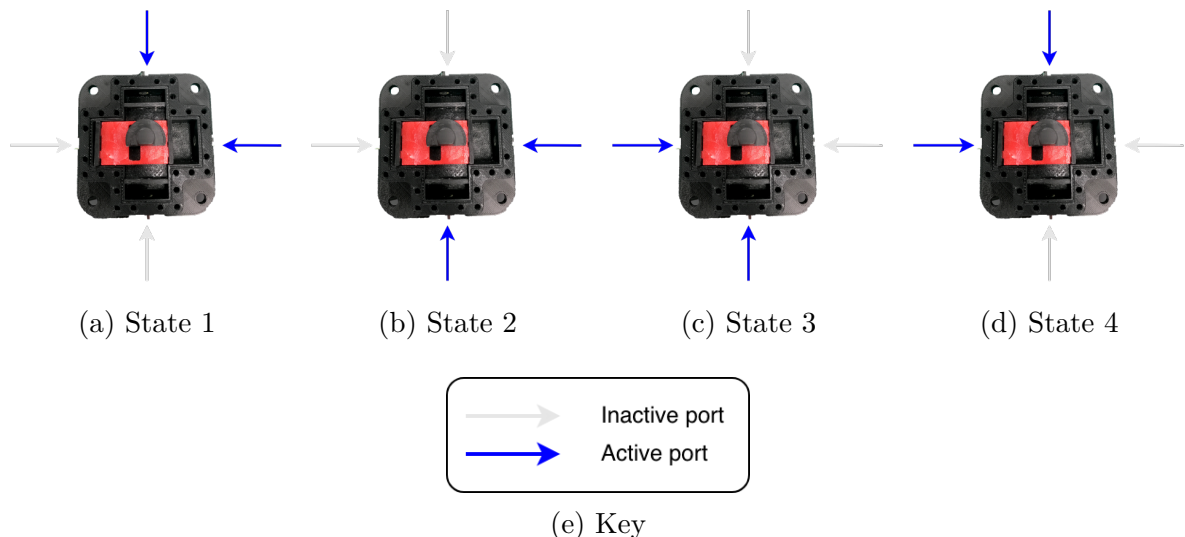


Figure 3.6: Switching the valves in the sequence 1-2-3-4 causes a clockwise rotation of the motor shaft

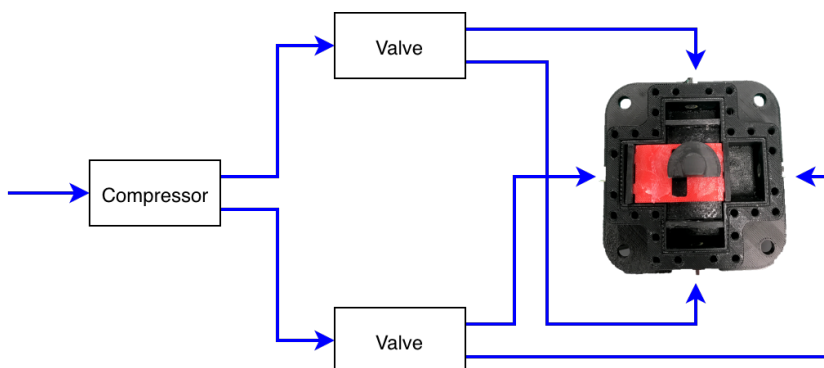


Figure 3.7: Pneumatic connections for the rotary stepper motor

¹An exchange student from Boston University who worked on this project in Semester 1 2018

Figure 3.7 shows pneumatic connections for the rotary stepper motor. Pressurised air from the compressor flowed into the two valves, which then directed the air into an outlet depending on the control signal from the Arduino. Each valve can only have one of its two outlets active at a time. For this pneumatic design to work, each valve must have its outlets connected to opposing sides of the stepper motor. There were no outlet ports on the motor to exhaust compressed air. Instead, air was exhausted through the cracks and crevices where the motor did not have an airtight seal, especially because the 3D-printed parts were slightly porous.

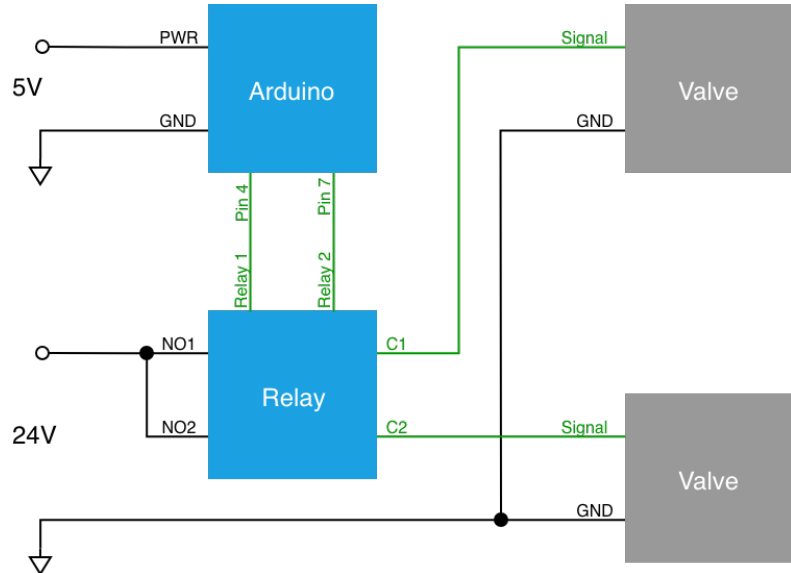


Figure 3.8: Electrical connections for the rotary stepper motor

Because the valves required a higher voltage and current output than could be supplied by the Arduino Due, we used an additional 24V power supply and relay to deliver power to the valves. These components were wired as shown in Figure 3.8.

Air motor

Air motors resemble DC motors in that they both have a rotating shaft that can produce continuous motion over a range of speeds. The air motor that we used was custom-made with non-ferromagnetic parts from the German manufacturer Deprag, as shown in Figure 3.9. The motor had two air inlets – one for each direction of rotation, clockwise and counterclockwise – and one air outlet to exhaust the compressed air. Increasing the pressure to either of the inlet ports increased the speed of shaft rotation.

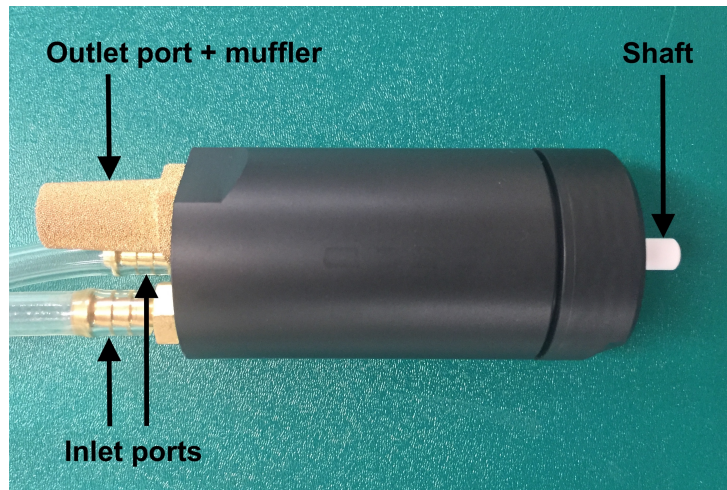


Figure 3.9: Deprag air motor

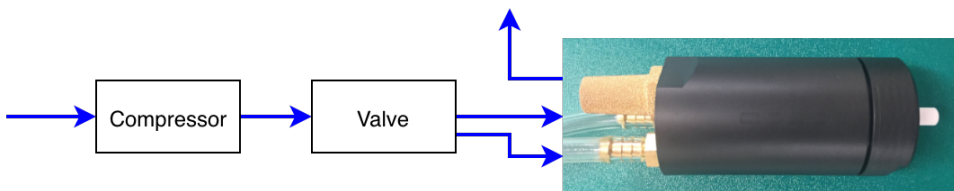


Figure 3.10: Pneumatic connections for the air motor

Figure 3.10 shows the pneumatic connections for the air motor. Due to the lack of a pneumatic pressure controller available, the design for this air motor was limited to just one valve which switched the direction of motion. With a fixed air pressure determined by the pressure gauge on the compressor, the motor operated at a fixed speed in both

directions of rotation. This led to a very simple electrical setup, which is shown in Figure 3.11.

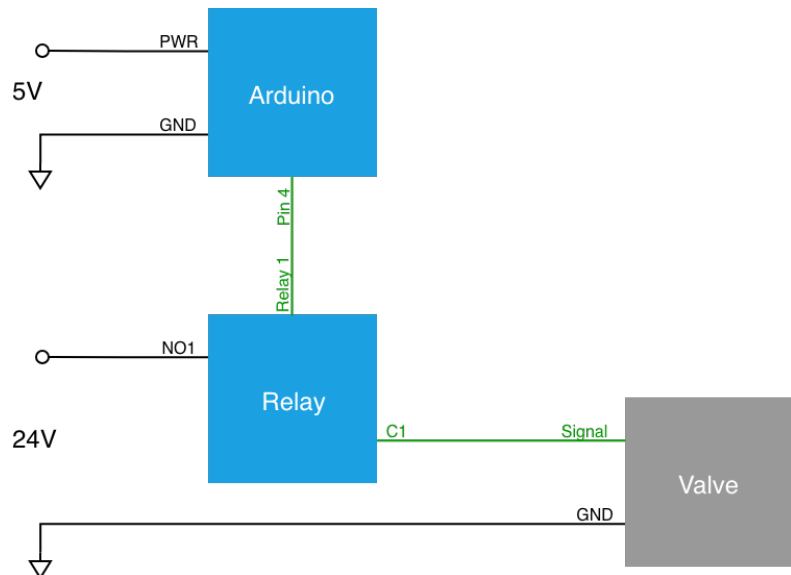


Figure 3.11: Electrical connections for the air motor

Double-acting cylinder

In a pneumatic cylinder, the compressed air caused a piston to extend and retract linearly. This was different from the previous two pneumatic motors which use compressed air to produce rotary motion. A double-acting cylinder has two ports. When one port becomes pressurised, the other port must act as an exhaust, and vice versa. The double-acting cylinder is shown in Figure 3.12.

Pneumatic cylinders are very simple to set up, except that the piston should never be allowed to reach its maximum extension or retraction. This is because an MR-compatible cylinder is made from glass², and the force of the compressed air can cause the pistons to damage the stoppers at either end of the cylinder. We have laser-cut acrylic sheets and built a jig to limit the stroke of the pneumatic cylinder.

²A conventional pneumatic cylinder would typically be made from metal and can be allowed to “bottom out”.

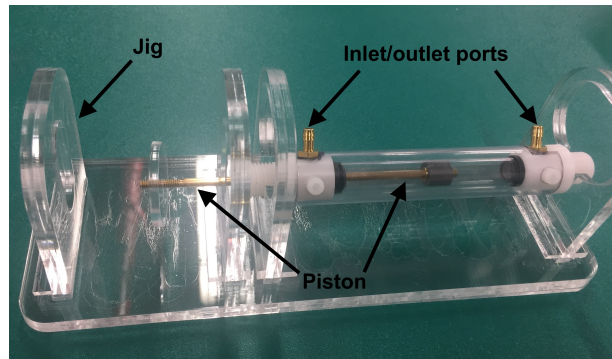


Figure 3.12: Double-acting cylinder

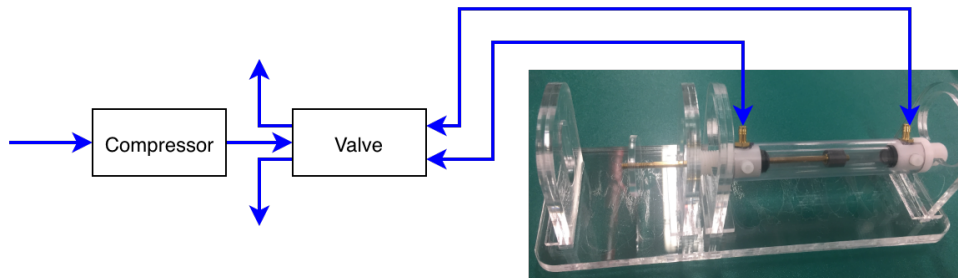


Figure 3.13: Pneumatic connections for the cylinder

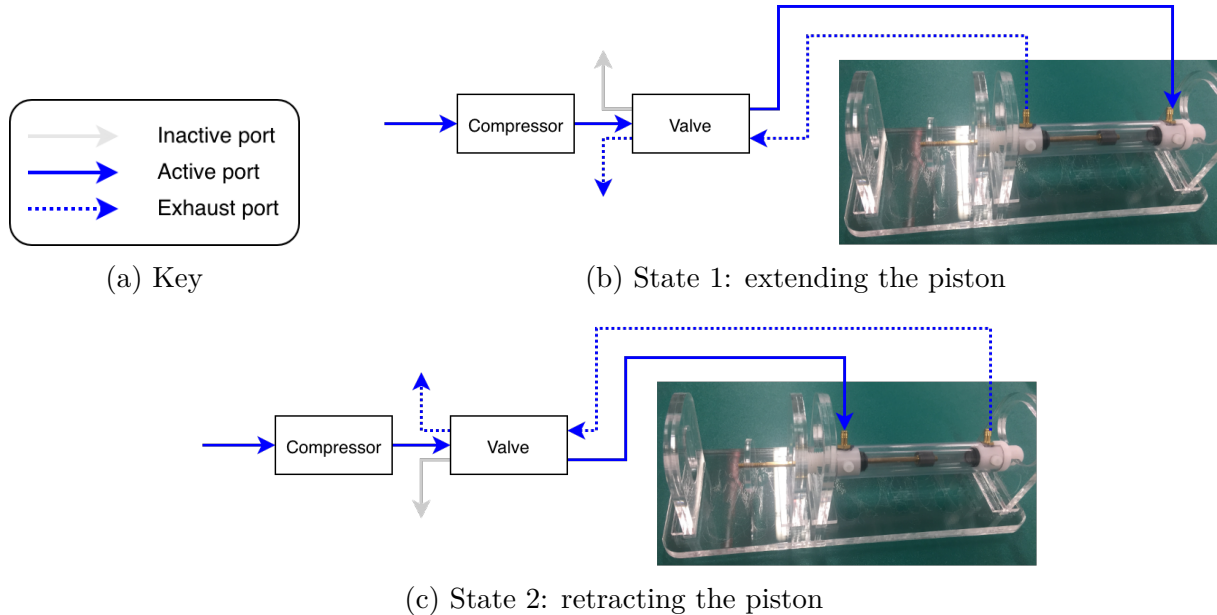


Figure 3.14: States in the pneumatic cylinder system

The pneumatic connections for the double-acting cylinder is shown in Figure 3.13. The two ports on the cylinder acted as both air inlets and outlets. Air was exhausted from the system through the the valves which have exhaust ports for when there is air flowing *into* one of its outlet ports. These operations are illustrated in Figure 3.14. The electrical system for the pneumatic system has the exact same configuration as the Deprag air motor (Figure 3.11).

3.2 SNR Analysis

As aforementioned, it has been reported that actuators can impact on scan image quality. To verify this claim, we assessed the impact of each actuator on image quality in terms of SNR. We visited two MRI facilities to perform a series of tests on two different scanners, which allowed us to produce more robust and reliable results. While our focus is on the MRI-LINAC, it was deemed useful to test on the 7T small animal system as well because higher magnetic field strength MRIs are more sensitive. The metric we measured was the SNR of a uniform phantom in the presence of each actuator during the scan.

The scan images were stored as DICOM files, which were then processed on MATLAB. When performing SNR calculations on the scan images, the phantom was defined as our simulated signal of interest for consistency in measurement – what we were really interested in measuring was the effect of our test items on the phantom SNR.

In addition to testing the four actuators described in Section 3.1, we also tested an optical encoder and a linear slide. While the encoder and linear slide are not actuators themselves, we decided to test them as well because they are common components that could potentially be built into a robotic system.

Many of these test items required peripheral equipment to power the device – e.g. controllers, drivers and valves– but most, if not all, of these devices were ferromagnetic and could not be placed inside an MRI scanner. Instead, the peripheral equipment remained

outside of the scan room, with only the essential wires and tubes being passed into the scan room via a waveguide. The equipment setup is illustrated in Figure 3.15

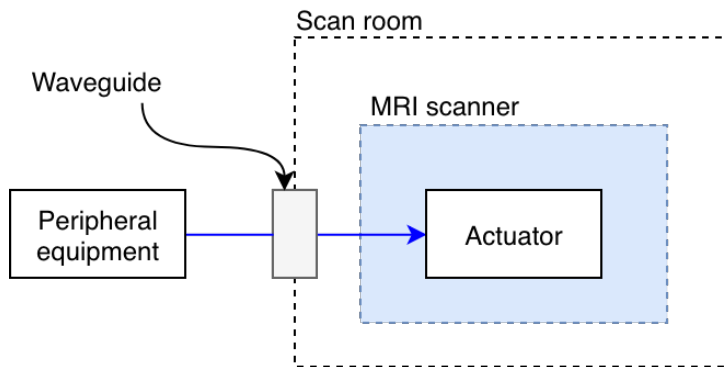


Figure 3.15: Equipment setup during test scans

Unfortunately, we could not test the ceramic motor system in closed loop because the jig was too big to fit into the 7T small animal system. Although it was ready to be tested on the 1.5 MRI-LINAC, we were not able to test the ceramic motor in closed loop control due to technical difficulties. Not being able to test the ceramic motor in closed loop meant that we could not quantify the SNR losses of the optical encoder and linear slide whilst moving, and could only test them as passive objects.

3.2.1 Testing SNR on the 7T small animal system

The first facility we tested on was the MR Solutions 7T small animal system at the University of Sydney Charles Perkins Centre. This scanner was designed for small animals (usually rodents), and was thus relatively small in size (see Figure 3.17). We first positioned a falcon tube in the middle of the RF coil to act as the uniform phantom, and then placed our test item as close as possible to the phantom without touching it. The field of view (FOV) slices through the middle of the phantom, as shown in Figure 3.16. The test items were positioned outside but adjacent to the FOV, which would still impact on the image SNR if there were any MR-incompatibility issues in the test item.

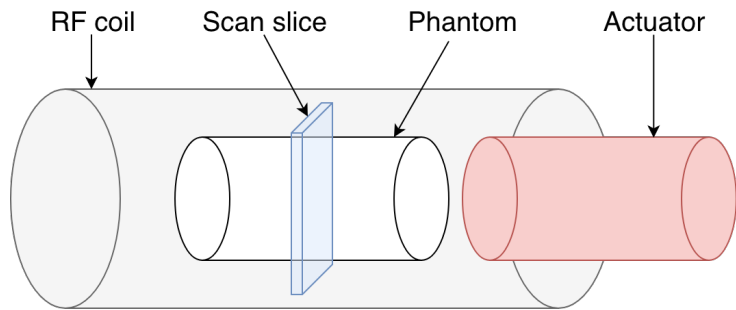


Figure 3.16: Phantom and scan slice setup

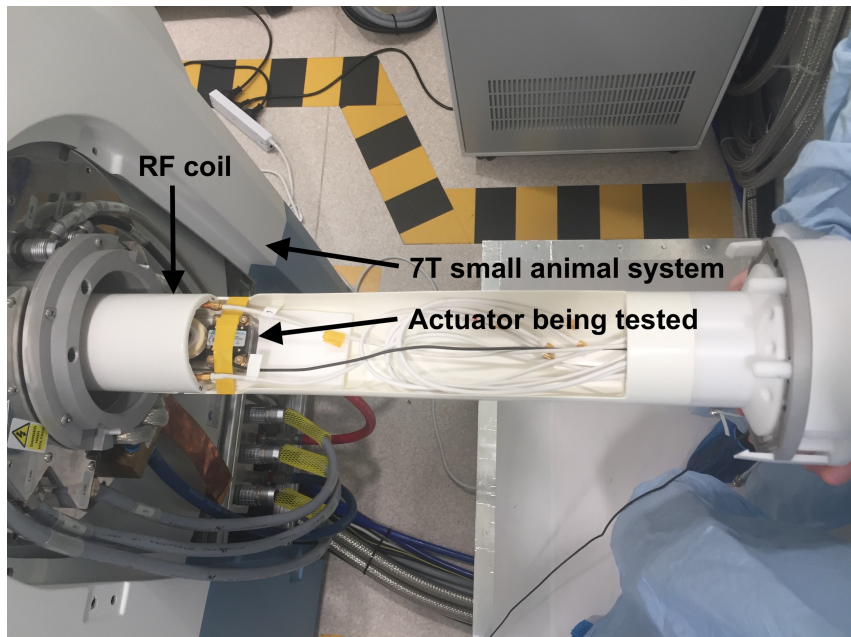


Figure 3.17: A ceramic motor is loaded at the edge of an RF coil, ready to be tested on the 7T scanner. Hidden from view is the falcon tube sitting in the middle of the RF coil.

Except for the rotary stepper motor, which was too large to fit inside the scanner, we were able to test the air motor, open-loop ceramic motor, cylinder, optical encoder, and linear slide. The configurations for each actuator are summarised in Table 3.4. For each configuration, we were able to take three scan images using a spin echo (SE) sequence. The scan parameters are listed in Table 3.5.

Table 3.4: Test configurations on the 7T small animal system

Item	Stationary	Moving
Air motor	✓	✓
Ceramic motor (open loop)	✓	✓
Cylinder	✓	✓
Optical encoder	✓	
Linear slide	✓	
Stepper motor		

Table 3.5: MRI scan parameters for our first test on the 7T small animal system

Scan parameter	Value
Sequence	SE
Repetition time	1000ms
Echo time	11ms
Slice thickness	3mm
Field of view	60mm x 60mm
Image resolution	128 x 256
Phantom type	water-filled falcon tube

While the air motor, cylinder, and stepper motor were scanned in the stationary configuration, the air compressor and valves were left switched. This is because in a realistic scenario, an actuator would still have its peripheral equipment powered on even during instances when the motor is stationary. Thus, if a motor was to demonstrate a decrease in SNR while moving compared to when it's stationary, the difference would be a result of the interaction between the actuator movement and the changing magnetic field gradient of an MRI scanner. The same is true for the ceramic motor: the drivers and controllers were left switched on during the stationary tests because the robotic platform is intended to be switched on for the duration of the benchmarking process.

Once we obtained the scan images, we then processed the images on MATLAB to produce a value for SNR. SNR was calculated as:

$$SNR = \frac{\mu_{signal}}{\sigma_{noise}}, \quad (3.1)$$

where μ_{signal} is the mean value inside the signal region of interest (ROI) and σ_{noise} is the standard deviation in a background ROI.

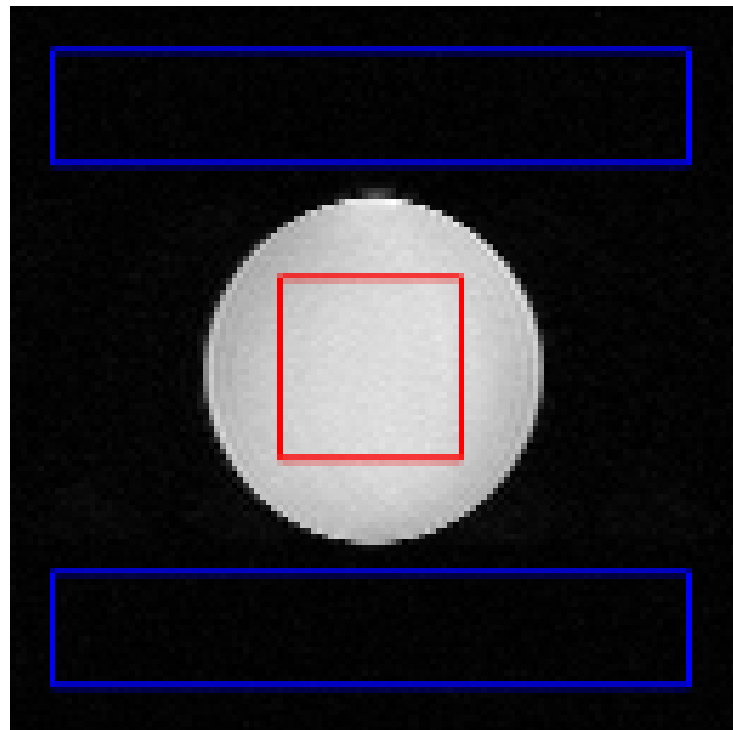


Figure 3.18: Red = signal ROI, blue = background noise ROIs

The ROIs used for the calculation are shown in Figure 3.18. The signal ROI was taken at the centre of the phantom, whilst the background ROI was taken as two horizontal rectangular boxes above and below the phantom. The signal and background ROIs were chosen based on the recommendations of the researchers who assisted our experiments and operated the 7T scanner.

3.2.2 Testing SNR on the 1.5T MRI-LINAC

The second facility we tested at was the 1.5T MRI-LINAC at the Ingham Institute in Liverpool, Sydney. We were able to test two different types of scan sequences on the 1.5T MRI-LINAC: SE and half-Fourier acquisition single-shot turbo spin-echo (HASTE).

1. SE: similar to the tests on the 7T small animal system, this sequence produced a single scan image acquired over a set scan duration.
2. HASTE: whereas the SE sequence produced a single scan image, the HASTE sequence can be thought of as the video equivalent of MRI scan images. Acquiring multiple scans over a longer duration of time allowed us to measure the change in SNR over time as we switch on/off different actuators. For our experiment, we switched on the motors halfway through the 60 second HASTE scan duration.

The scan parameters for each of these sequences are presented in Tables 3.6 and 3.7.

Table 3.6: MRI scan parameters for SE sequence on the 1.5T MRI-LINAC

Scan parameter	Value
Sequence	SE
Repetition time	1000ms
Echo time	30ms
Slice thickness	5mm
Field of view	300mm x 300mm
Image resolution	256 x 256
Phantom type	gadolinium-doped water-filled sphere

Table 3.7: MRI scan parameters for HASTE sequence on the 1.5T MRI-LINAC

Scan parameter	Value
Sequence	HASTE
Repetition time	500ms
Echo time	98ms
Slice thickness	5mm
Field of view	300mm x 300mm
Image resolution	128 x 128
Number of frames	120
Phantom type	gadolinium-doped water-filled sphere

Similar to our experiments on the 7T small animal system, the phantom was the signal of interest, and was placed at the centre of the FOV. For this set of experiments, we used a gadolinium-doped water-filled sphere as the uniform phantom. Also, the RF coil is much larger in the MRI-LINAC because it is designed to fit human patients, so all the components were able to fit very comfortably, including the rotary stepper motor, which did not fit inside the 7T small animal system. The configurations for each actuator are presented in Figure 3.8

Table 3.8: Test configurations on the 1.5T MRI-LINAC

Item	Stationary	Moving
Air motor	✓	✓
Ceramic motor (open loop)	✓	✓
Cylinder	✓	✓
Optical encoder	✓	
Linear slide	✓	
Stepper motor	✓	✓

The SNR of each actuator was calculated using the dual acquisition, subtraction method proposed by Firbank et al [37]. This method uses two consecutive scans under the same conditions to acquire a single measurement for SNR, with the first scan acting as the signal image. Subtracting the second scan from the first scan then produces a subtraction image, which is taken to be the noise profile. The formula to determine SNR is defined as:

$$SNR = \sqrt{2} \frac{\mu_1}{\sigma_{1-2}}, \quad (3.2)$$

where μ_1 is the mean intensity in the signal ROI of the first scan and σ_{1-2} is the standard deviation in the noise ROI of the subtraction image [37]. An example of the scans and ROIs used in one SNR calculation are presented in Figure 3.19.

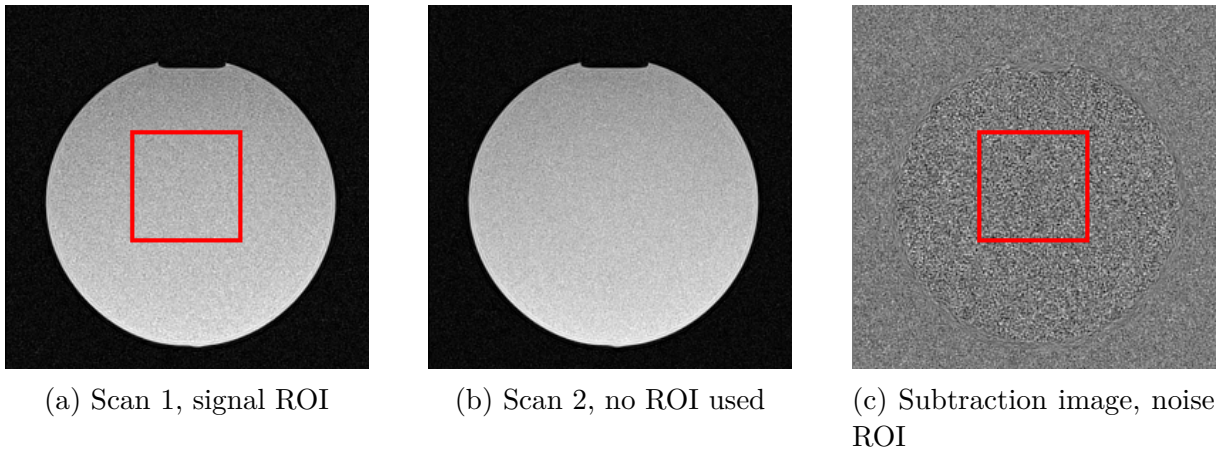


Figure 3.19: An example of scans used for SNR calculation

This method of calculating SNR was the standard procedure used by the researchers who work with the 1.5T MRI-LINAC. Note that this is different from the standard procedure recommended to us for the 7T small animal system experimental data.

3.3 Prototyping a pneumatic stepper motor

Having built and tested a ceramic motor and three pneumatic actuators, the next natural progression was to begin thinking about how a multi-axis robotic platform would look and what type of actuators can be scaled into the platform. From the results of our SNR analysis (see Section 4.2), it was deemed reasonable to rule out ceramic motors and pursue pneumatic actuators instead, the main reason being that ceramic motors consistently exhibited the worst SNR performance across all three sets of experiments. Pneumatic actuation devices, on the other hand, demonstrated excellent MR-compatibility with minimal impact on image SNR.

For this next part of the project, there were two main sources of inspiration that guided the design of a pneumatic prototype actuator. The first was a pneumatic stepper motor design which Groenhuis et al. [26] used in their needle insertion robots, as illustrated in Figure 3.20. What's special about this type of motor is that it exploits the switching of valves to drive the motor in discrete steps, thereby minimising the complexities of pneumatic control that would arise from trying to drive a motor through continuous control of pressure. Groenhuis et al. [26] have also demonstrated a curvilinear stepper motor in their most recent needle insertion robot design (Figure 3.20b).

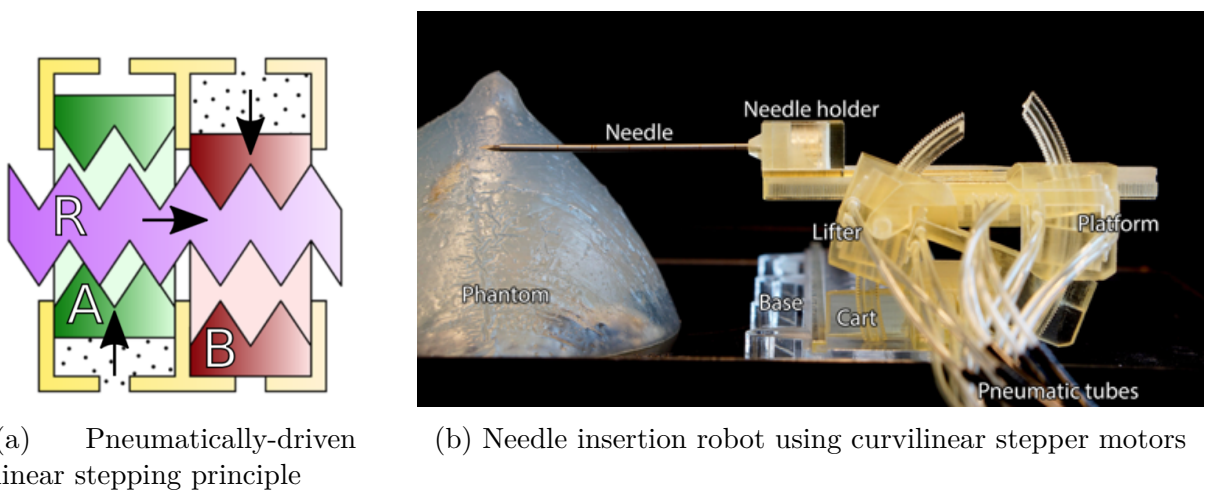
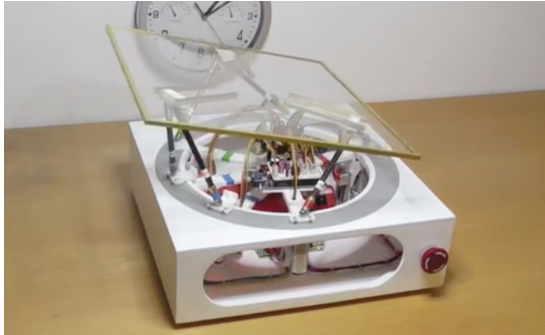


Figure 3.20: Stepper motors designed by Groenhuis et al. [26]

In the case of continuous control of pressure, there is the problem of compressibility of air and the transport delay as compressed air flows through the pneumatic lines which make feedback control difficult. In a stepper motor, transport delay and air compressibility is still a problem, but can be mitigated by setting the pressure above a minimum operating level where the motor can be expected to behave consistently.

The goal of this project was to work towards a robotic platform that can manipulate a phantom, which differs from a needle insertion robot in both its payload and the range of motion required. In the spirit of exploration and novelty, the latter half of this project involved combining the stepping principle demonstrated by Groenhuis et al. with an unconventional Stewart platform design by an anonymous Youtube video [38], which named their design a circular base Stewart platform.



(a) A circular base Stewart platform. The legs have fixed lengths but are able to slide around a circular track.



(b) Underside view of Stewart platform – each leg is attached to a motor which drives the legs around the track.

Figure 3.21: Circular base Stewart platform [38]

In a traditional Stewart platform, each of the six legs can independently extend and retract, which then causes the plate that rests on the six legs to change position and orientation. On the other hand, the circular base Stewart platform demonstrates a different type of Stewart platform where the legs have fixed lengths but are able to slide around a circular track, as shown in Figure 3.21. This model was not designed for an MR environment, however, and needed some tweaking to make a pneumatic version of the circular base Stewart platform.

3.3.1 Proof of concept

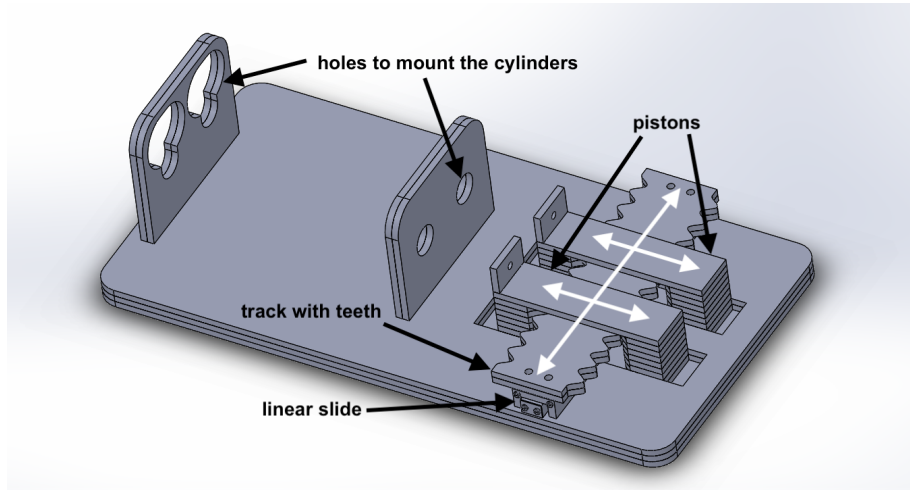


Figure 3.22: A jig to demonstrate the stepping mechanism

The model shown in Figure 3.22 was designed as a proof of concept to demonstrate the stepping mechanism that Groenhuis et al. [26] used in their designs. For our proof of concept, the idea was to use existing parts we already had at hand and make a quick and dirty prototype. Instead of using four pressurised chambers, this proof of concept used two pneumatic cylinders to drive the “pistons”, which are technically no longer pistons as there is also no longer a chamber that contains the “pistons”. A track with sinusoidal teeth was then mounted on the carriage of a linear slide to restrict the track to lateral movement.

3.3.2 Curvilinear stepper motor

We then began prototyping a curvilinear stepper motor on Solidworks. Because the stepper motor had to be mounted on a fixed circular track, there was an opening in the motor housing to allow the track to protrude from the bottom so that the track could rest on a surface. This is different from Groenhui et al.’s stepper motor which enclosed the track completely on both sides.

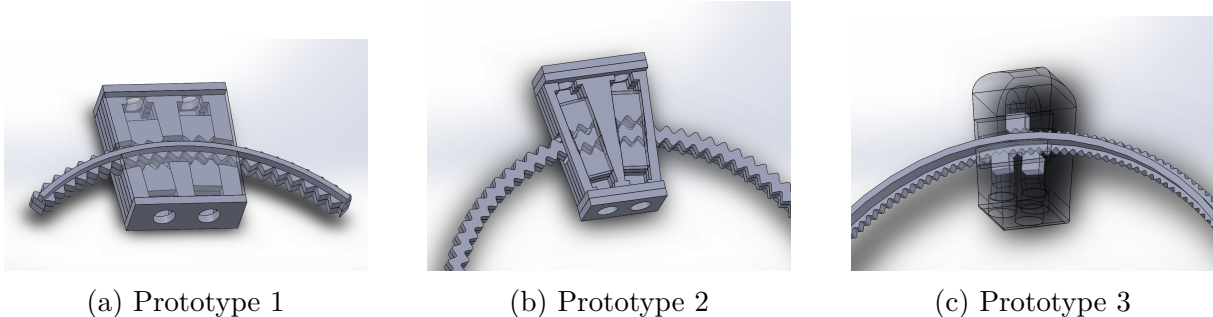


Figure 3.23: Three different iterations of design for a curvilinear stepper motor

The first two prototypes in Figure 3.23 have four chambers and pistons, which were connected so that the pistons move in pairs. Pressurising each chamber in a sequential pattern caused the motor to move around the circular track. If each time a new chamber is pressurised is called a ‘step’, then it takes four steps for the motor to traverse one tooth arc in the sinusoidal track.

The third prototype in Figure 3.23 was similar to the first two prototypes except that there were three individual chambers and pistons and it took three steps to traverse one tooth arc in the sinusoidal track. Also, one of the chambers wrapped around to the other side of the motor so that the inlet ports were all on the same face on the motor for the sake of better tube management. The motor housing was slightly thicker for this prototype due to the wrapping of the inlet port.

3.3.3 Circular track

The stepper motor straddled a circular sinusoidal track shown in Figure 3.24, which was used to guide the motor as well as provide the teeth which the pistons could mesh with. The sinusoidal portion was enclosed by the motor housing, whilst the smooth circular portion was the part of the track that extruded out from the motor.

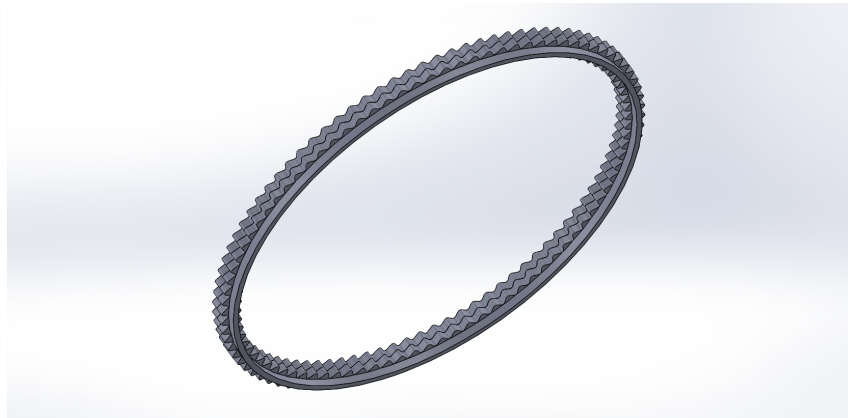


Figure 3.24: Circular track with sinusoidal teeth

The sinusoidal track geometry was defined by two circular standing waves, which were subsequently defined by the parametric equations:

$$x = (R + a \cdot \sin(n\theta)) \cdot \cos(\theta) \quad (3.3)$$

$$y = (R + a \cdot \sin(n\theta)) \cdot \sin(\theta) \quad (3.4)$$

where R is the radius of the circle (mm), a is the amplitude of the standing waves (mm), n is the number of waves in a revolution, and θ is the parameter. Increasing R increases the size of the track, a determines the depth of the teeth, and n determines the step angle subtended by each tooth in the circular track. For the track prototype that we developed, the variables took on the values:

Table 3.9: Values for the standing wave parameters in the sinusoidal circular track.

Variable	Inner curve	Outer curve
R (mm)	75	80
a (mm)	1.25	1.25
n	90	90
θ	0 to 2π	0 to 2π

3.3.4 Mechanical stepping pattern

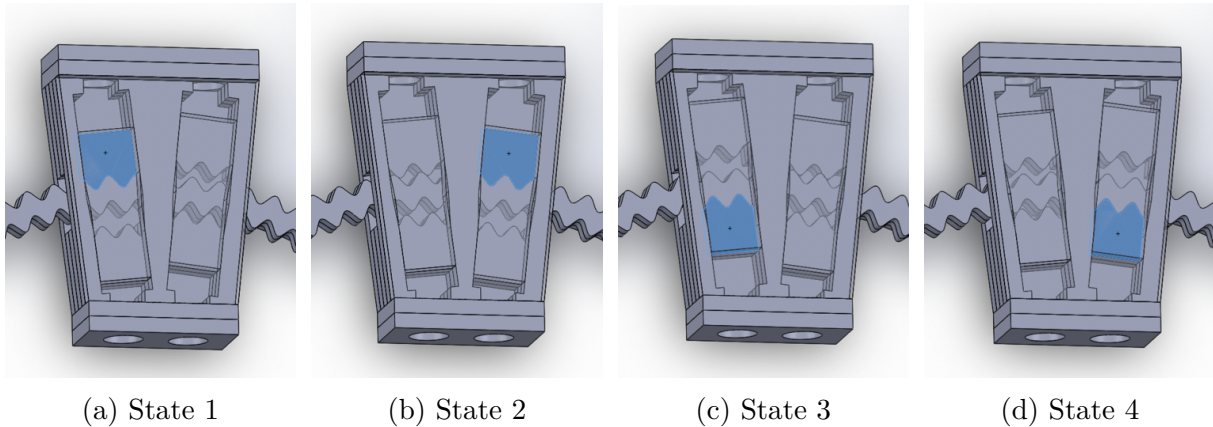


Figure 3.25: Stepping mechanism of a pneumatic curvilinear stepper motor

As seen in Figure 3.25, there are four possible states in the curvilinear stepper motor. In state 1, the first piston is engaged. In state 2, the first piston becomes disengaged when the second piston becomes engaged. In state 3, the second piston becomes disengaged when the third piston is engaged. Lastly, in state 4, the third piston becomes disengaged when the fourth piston becomes engaged. In four steps, the motor will travel one tooth arc length.

A cycle is defined as: 1 cycle = 1 tooth arc = 4 steps. Since there are 90 cycles distributed around the circular track (see row n in Table 3.9), and each cycle has 4 steps, then there are 360 steps distributed around the circular track. Therefore, each step in the curvilinear stepper motor causes a 1° traversal across the arc of the circular track.

3.3.5 Fabrication

To turn the Solidworks prototypes into real-life models, we used two types of fabrication techniques that made sense for this prototype and were readily available at the AMME Fabrication Laboratory.

Laser cut acrylic

One fabrication method we used was to laser cut sheets of acrylic into the appropriate shape and then superglue the layers together to form 3D parts. These layers are shown in Figure 3.26. Each part was then sanded down lightly where smooth surfaces were critical, e.g. the piston and chamber surfaces, or the surfaces where the track is in contact with the motor housing. Acrylic was chosen over medium-density fibreboard (the only other freely available material) because of the smoother surface finish of acrylic.

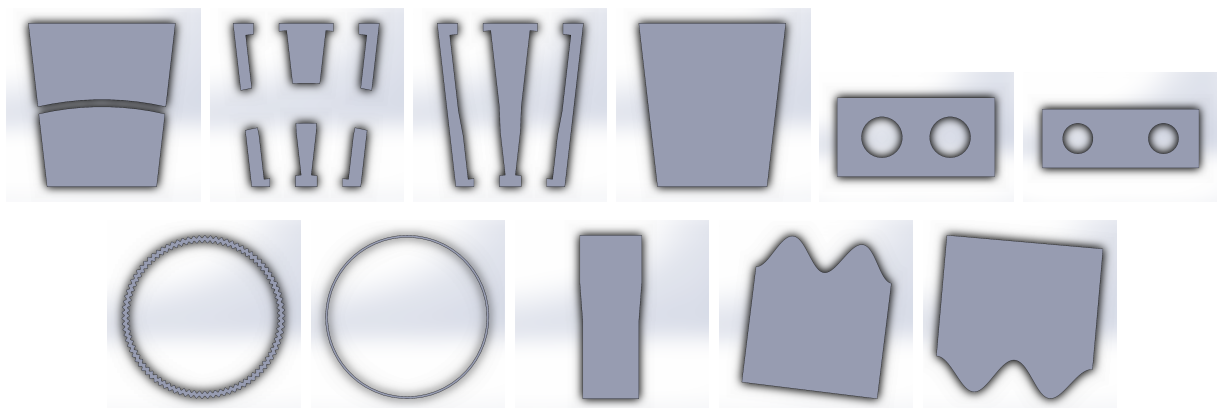


Figure 3.26: Example of all the distinct layers required for the prototype in Figure 3.25b (relative sizes are not to scale)

Resin stereolithography

Another method of fabrication that we tested was stereolithography, i.e. 3D-printing resin. In stereolithography, a laser is aimed into a vat of resin, which semi-cures the resin layer-by-layer into a solid and can achieve micron-level layer thicknesses. The benefit of stereolithography is that it can generate very precise models which have a solid body, compared to fused deposition modelling of plastic filaments (the more common 3D-printing method). A solid body is useful when attempting to create an airtight seal in the chambers of a pneumatic stepper motor. Stereolithography did not require the Solidworks prototype to be split into a number of layers and superglued together – most of the parts can be fabricated in one piece.

After removing the semi-cured model from the printer, the model was immersed in isopropyl alcohol for 10 minutes to dissolve the excess uncured resin. The supports generated in the printing process were then snapped off. Then, the model was dried off and placed into a UV chamber for 10 to 30 minutes depending on the thickness of the parts. Finally, we sanded down the surfaces, especially where the supports did not break off cleanly.

3.3.6 Pneumatic control

For the four-chamber prototype in Figure 3.23, each piston must mesh fully with the track independently of the other three pistons, which meant that only one chamber could be pressurised at a time. Figure 3.27 shows electrical and pneumatic connections we used to pressurise only one out of four chambers at a time.

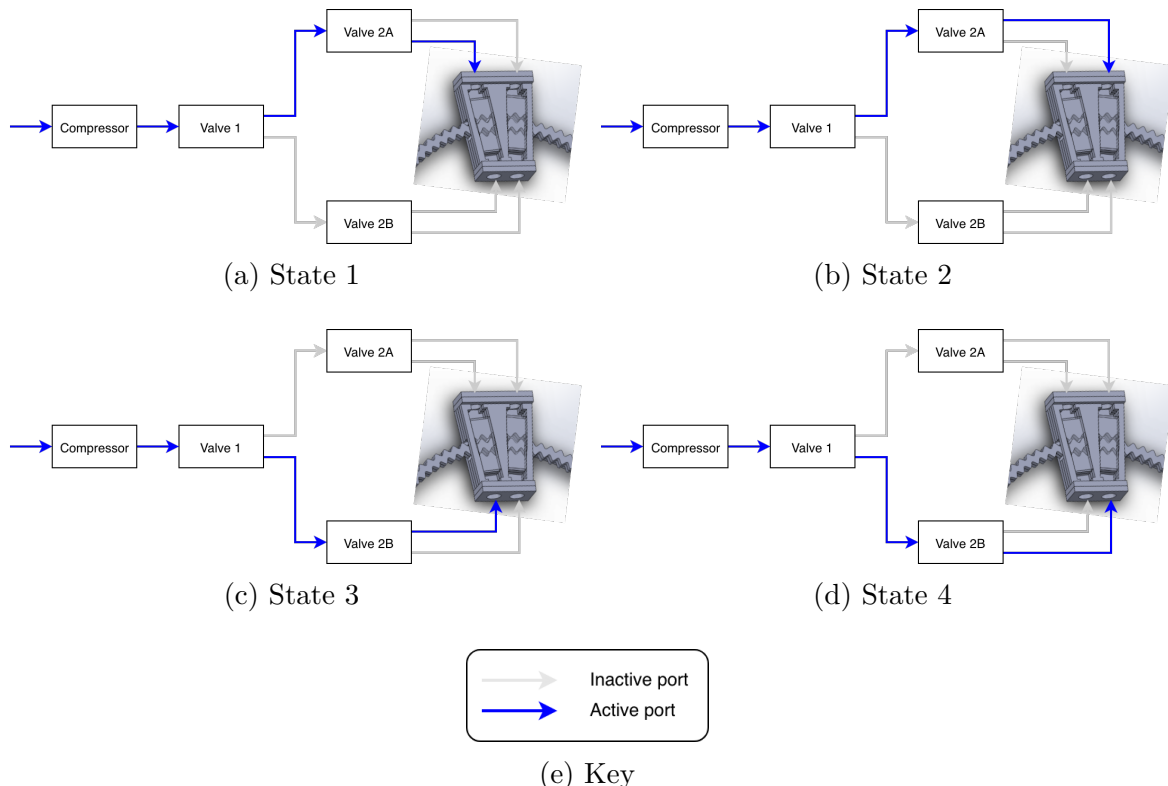


Figure 3.27: Switching the valves in the sequence state 1-2-3-4 produced a counterclockwise movement of the motor relative to the circular track. Switching in the sequence state 4-3-2-1 produced a clockwise movement of the motor relative to the track.

State	Valve 1	Valve 2A/B
1	Outlet 1	Outlet 1
2	Outlet 1	Outlet 2
3	Outlet 2	Outlet 1
4	Outlet 2	Outlet 2

Table 3.10: Activated outlet ports in each valve for each system state

Figure 3.28 shows the electrical connections for the four-chamber prototype. Note that the valves labelled 2A and 2B share the same control signal, but are not pneumatically tethered together (see Figure 3.27). Under this configuration, the control of the 4-chamber prototype was very simple: valve 1 switched at half the frequency of valves 2A/B.

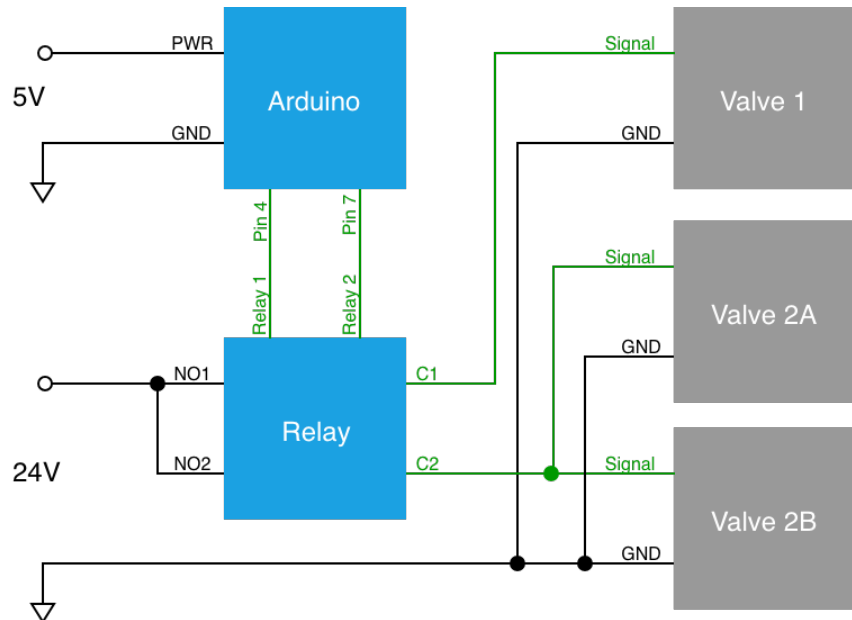


Figure 3.28: Electrical connections for the four-chamber prototype actuator

3.4 Actuator Characterisation

In the previous section, we have prototyped a series of curvilinear stepper motors. This section describes the next logical step in the process: to elect the best prototype and characterise its performance in order to understand its scalability into a multi-axis robotic platform. It was through a few iterations of design-build-test, that the second acrylic prototype emerged as the best motor to continue investigating. Thus, we devised a simple yet effective pulley system with which tested the load and bandwidth performance of our prototype actuator. The overall experimental setup is shown in Figure 3.29, and a close-up view in Figure 3.30.

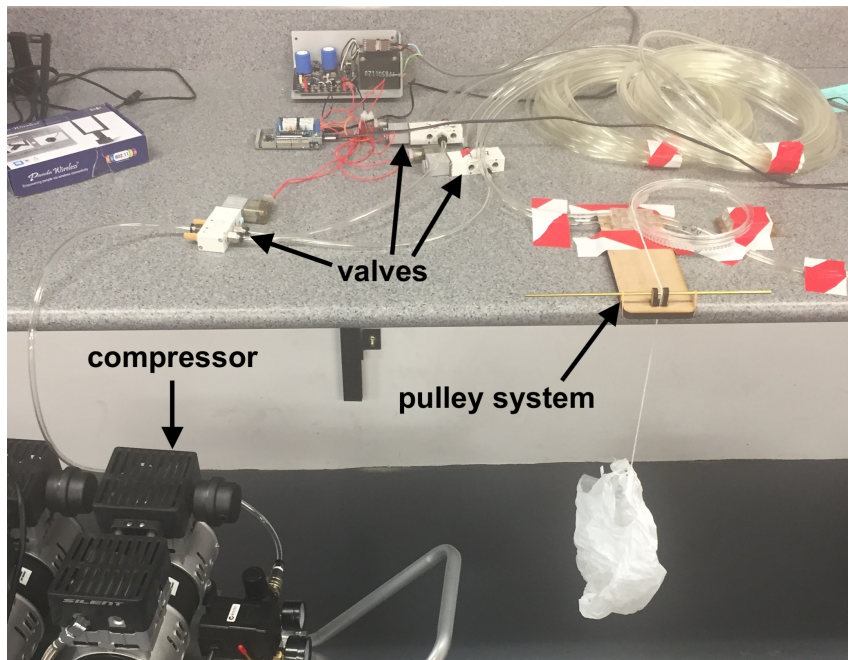


Figure 3.29: Bench-top setup for load and bandwidth tests. A bag is tethered to the end of the pulley system to hold the weights.

In this pulley system, the actuator was stationary while the track rotated to raise and lower the bag of weights. As the actuator raised the weights, it also had to overcome the frictional forces of:

- The track in contact with the motor and the track support

- The pistons in contact with its chambers and the track teeth
- The string as it slid across the brass bar

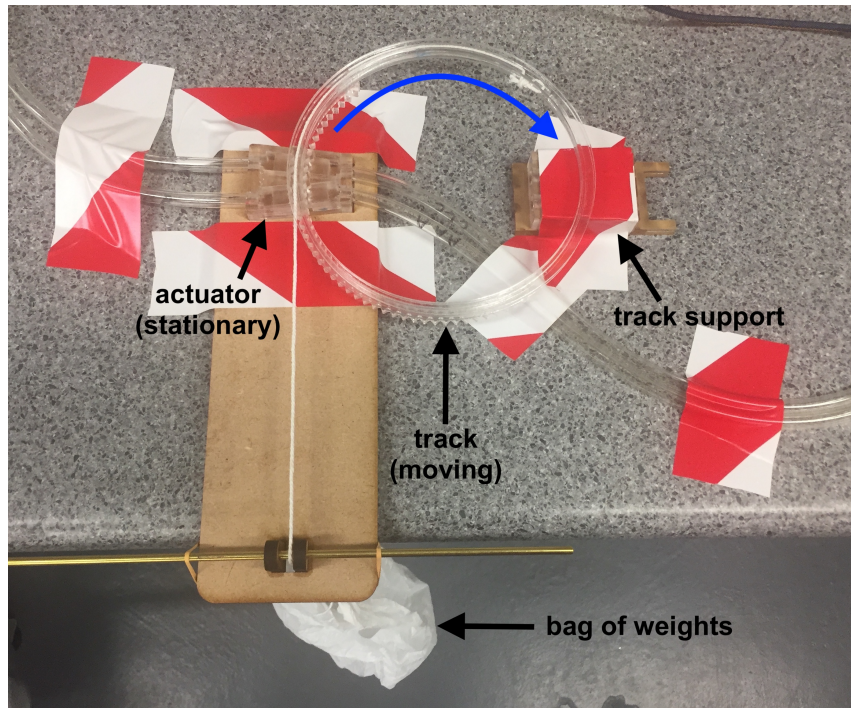


Figure 3.30: Close up of the pulley system

While the frictional forces in the system are unknown, we can however quantify the additional load of the weights acting tangentially to the circular track. The values of the known masses in the system are listed in Table 3.11.

Item	Mass (g)
Bag	5
Weights (AAA batteries)	11
Track + string	42

Table 3.11: Known masses in the pulley system

3.4.1 Load tests

Load tests were conducted by driving the motor at a low step frequency and then adding weights to the pulley system until the motor stalled. The actuator was loaded with an initial mass of 47g from the track and the bag. What is being tested here was the *additional* load added to the system before the motor stalled. AAA batteries (11g each) were used to increment the weights.

First, the compressor gauge was fixed at 1 bar pressure. Then, the motor was operated through 10 cycles³ clockwise and then another 10 cycles counterclockwise. The reason the motor was clocked for 10 cycles in either direction is because the friction profile is not consistent for the whole arc length of the track, nor for each piston, so testing over a wider arc length would produce more consistent results between trials.

If at any point in the twenty cycles of operation the motor skipped a step or became stuck in one position, the motor was considered stalled. If the motor did not stall, a weight would be added to the pulley system and the twenty cycles would be repeated until the motor stalled. The total weight of all the batteries at stalling was considered the stall load. The whole experiment was then repeated for a variety of pressures from 1 bar to 3 bar in increments of 0.25 bar.

Stall load was given by the equation:

$$L = \left(\frac{2n - 1}{2} \right) m_b g, \quad (3.5)$$

where L is the stall load (N), and n is the number of batteries at which the motor stalled, m_b is the mass of the battery weights (kg), and g is gravitational acceleration at the Earth's surface ($9.806\,65\text{ m s}^{-2}$). The factor $2n - 1$ arose from the fact that the actual motor stalling occurs between $n - 1$ and n batteries. The parameters for the load test are listed in Table 3.12.

³Reminder: 1 cycle = 1 tooth arc = 4 steps

Parameter	Value
Stepping frequency	1 Hz
Pressures tested	1 bar - 3 bar
Pressure increments	0.25 bar
Initial mass	47g
Mass of weight increments	11g
Cycles per test	10 clockwise; 10 counterclockwise

Table 3.12: Experimental parameters for the load tests

3.4.2 Bandwidth tests

A bandwidth test was devised to determine the stepping frequencies the prototype actuator were able to achieve, which also gave an indication of the speeds the actuator was capable of. To maintain consistency with the load tests, the actuator was initially loaded with the weight of the track and the bag, though no additional battery weights were necessary for the bandwidth tests.

Bandwidth was tested for a range of pressures by decreasing the duration between steps until the motor stalled. The definition for motor stalling was the same as for the load tests – i.e. when the motor missed a step or became stuck during a 20 cycle run. Whenever the actuator was able to complete a 20 cycle run successfully, the step duration was decreased by 2ms. Once the actuator reached a stall frequency, the whole experiment was repeated for a different pressure level.

Bandwidth was then calculated as:

$$f = \frac{1}{2} \left(\frac{1}{t} + \frac{1}{t - 0.002} \right), \quad (3.6)$$

where f is the maximum stepping frequency of the actuator (Hz), and t is the stepping duration at which the motor stalls (s). f is thus the average of the upper and lower

bounds for measured maximum frequency due to the increment size of 2ms during the experiment. The parameters for the bandwidth test are listed in Table 3.13.

Parameter	Value
Pressures tested	1 bar - 3 bar
Pressure increments	0.25 bar
Initial mass	47g
Step duration decrements	2ms
Cycles per test	10 clockwise; 10 counterclockwise

Table 3.13: Experimental parameters for the bandwidth tests

Chapter 4

Results

4.1 Preliminary actuator implementation

In this section, we will describe some of the performance characteristics observed during the preliminary evaluation of actuators.

4.1.1 Ceramic motor

The ceramic motor was successfully actuated to drive the ceramic bearing at approximately 1.5 revolutions/second in the open loop setting. In the closed loop setting, we were able to achieve point-to-point position control of the linear slide carriage, which was driven back and forth along its track once every two seconds.

4.1.2 Pneumatic actuators

Rotary stepper motor

The rotary stepper motor was able to rotate its shaft in 90° increments with a nominal working pressure of 2 bar. The motor was capable of reaching 10 Hz stepping frequency

at this pressure.

Air motor

The air motor has a minimum operating pressure level of about 1.5 bar¹, above which the motor was able to rotate its shaft in both direction. Below this approximate minimum pressure level, the motor would either not start up at all or would stall during its operation.

Cylinder

The pneumatic cylinder performed binarised, end-to-end movements of its piston. The cylinder also had a minimum operating pressure level of around 1.5 bar¹.

4.2 SNR Analysis Results

4.2.1 7T small animal system

Figure 4.1 shows the SNR results for each actuator type from the 7T small animal system, and Figures 4.2 and 4.3 show example scans. The SNR performance of the moving air motor, whilst mild in SNR reduction, demonstrated a greater standard deviation in its results (Figure 4.1) than in all other test items. One plausible explanation for the variability in the moving air motor results is that the vibrations from the air motor caused a ringing artefact, which is related to the movement of a scan subject. The vibrating movements of the air motor are unpredictable and irregular, resulting in a scan image that is inconsistent between scans. Although all the scan images exhibit a small amount of ringing echo, this artefact is exacerbated in the moving air motor tests. In Figure 4.3, the ringing artefacts are excessive, even when compared to other moving test items.

¹Number obtained through experience than through experiment.

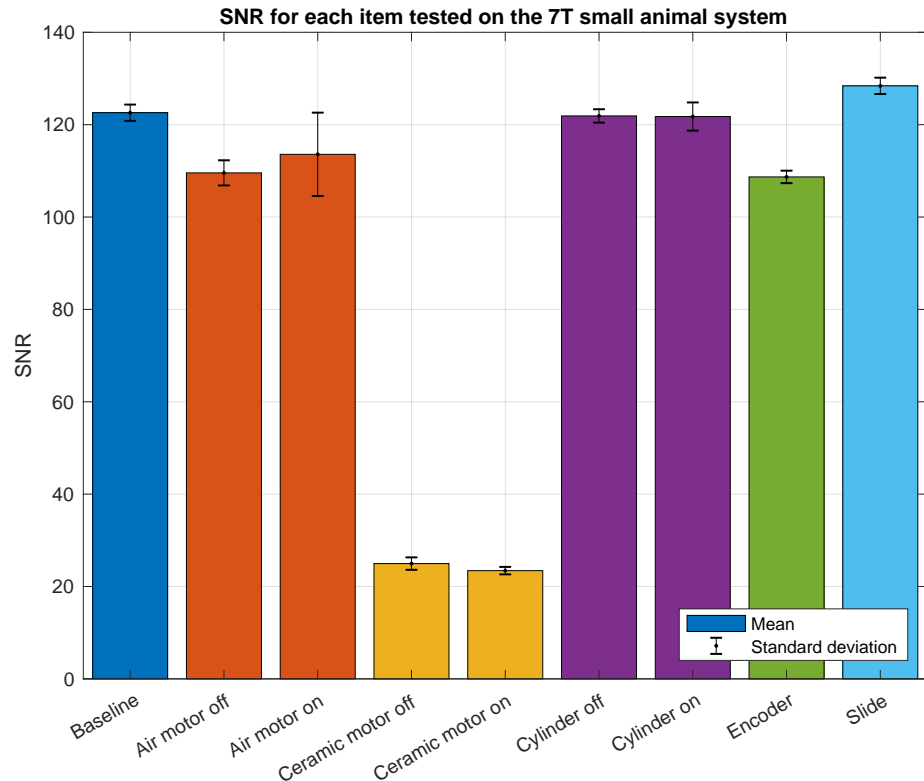


Figure 4.1: SNR results from the 7T small animal system

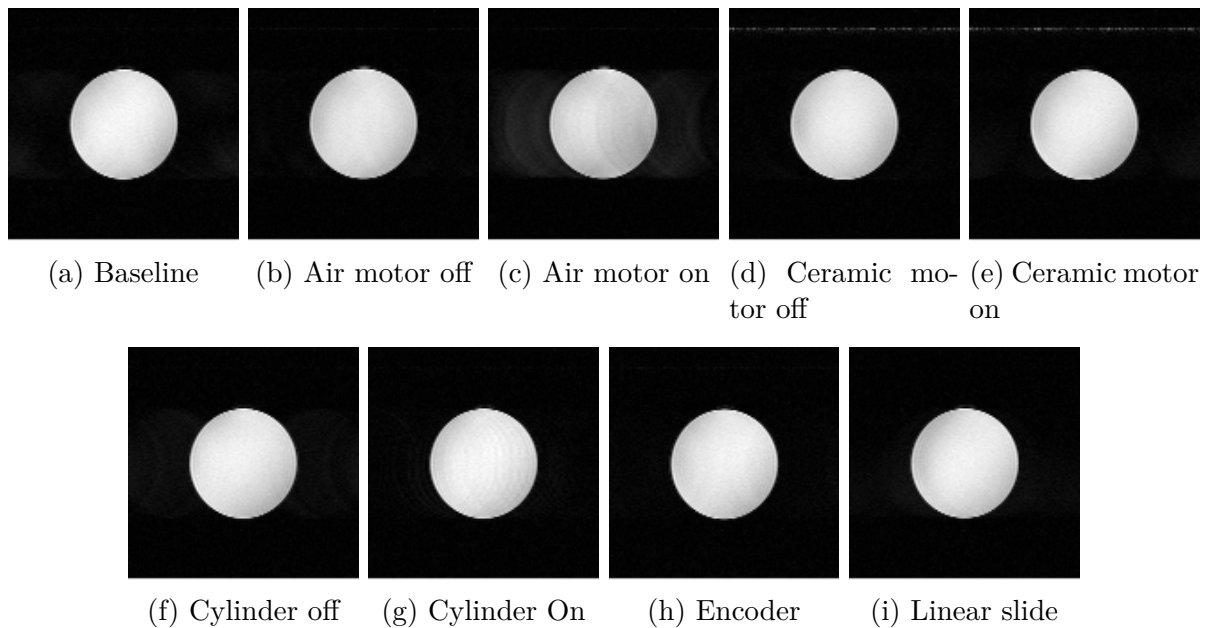


Figure 4.2: Sample original scan images from the 7T small animal system

In the ceramic motor scan images for both stationary and moving configurations, there is a white line at the top of the image, which suggests RF interference. Small amounts of RF interference is observable in the other images in Figure 4.3, but is much more severe for the ceramic motor scans. Because the ceramic motor operates on a high-voltage low-current sinusoidal signal, the RF interference artefacts are likely to be a result of the interaction of the motor signal frequency and the MRI resonant frequency. The SNR results for the ceramic motor were consistently poor compared to the inconsistently decent results of the moving air motor due to the localisation of the RF interference artefact within a small region in the scan and consistency of the interference pattern itself between scans.

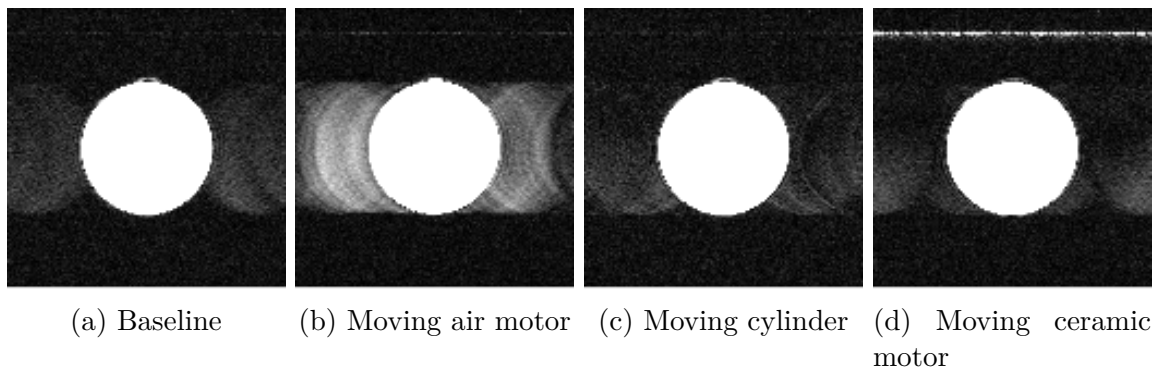


Figure 4.3: Sample scan images from the 7T small animal system with contrast adjusted to emphasise the image artefacts.

On the 7T small animal system, SNR analysis demonstrates that:

- The pneumatic cylinder in both off and on configurations and the stationary linear slide exhibit minimal reductions in SNR,
- The air motor in the off configuration and the stationary optical encoder exhibit mild, but still insignificant, reductions in SNR,
- The ceramic motor in both off and on configurations exhibit a significant decrease in SNR,
- The passive optical encoder and linear slide demonstrate good MR-compatibility.

4.2.2 1.5T MRI-LINAC

The SNR results for the 1.5T MRI-LINAC system are shown in Figure 4.4, and example scans are shown in Figure 4.5. The SNR analysis results from the 1.5T MRI-LINAC experiments demonstrate similar findings to the 7T small animal system results. The pneumatic systems cause minimal degradation in SNR while the ceramic motors cause a moderate reduction when stationary and a drastic reduction when moving.

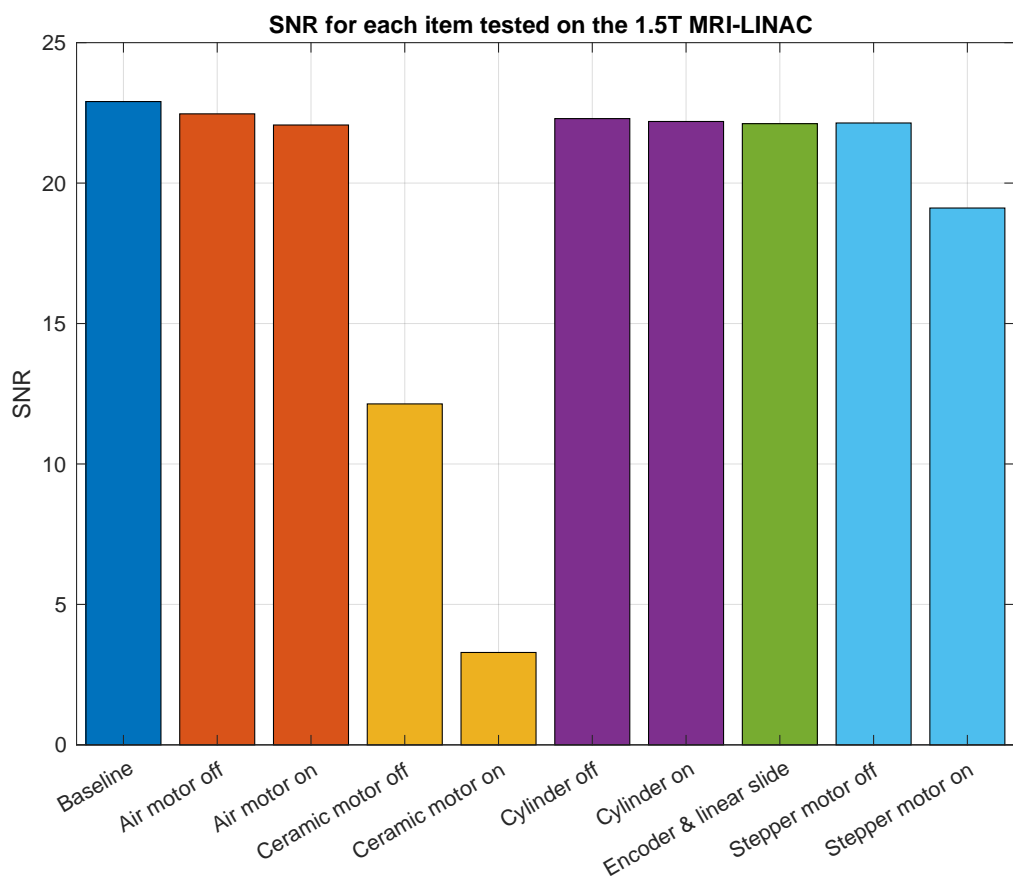


Figure 4.4: SNR results from the 1.5T MRI-LINAC (SE scans)

Unlike the 7T results, the air motor in a moving configuration did not exhibit a ringing effect from motion instability. Whereas in the 7T small animal system the air motor is partially inserted into the RF coil and is in direct contact with the coil, in the 1.5T MRI-LINAC, the air motor was only in contact with the relatively stable scan bed and

any transference of vibrations to the RF coil were negligible.

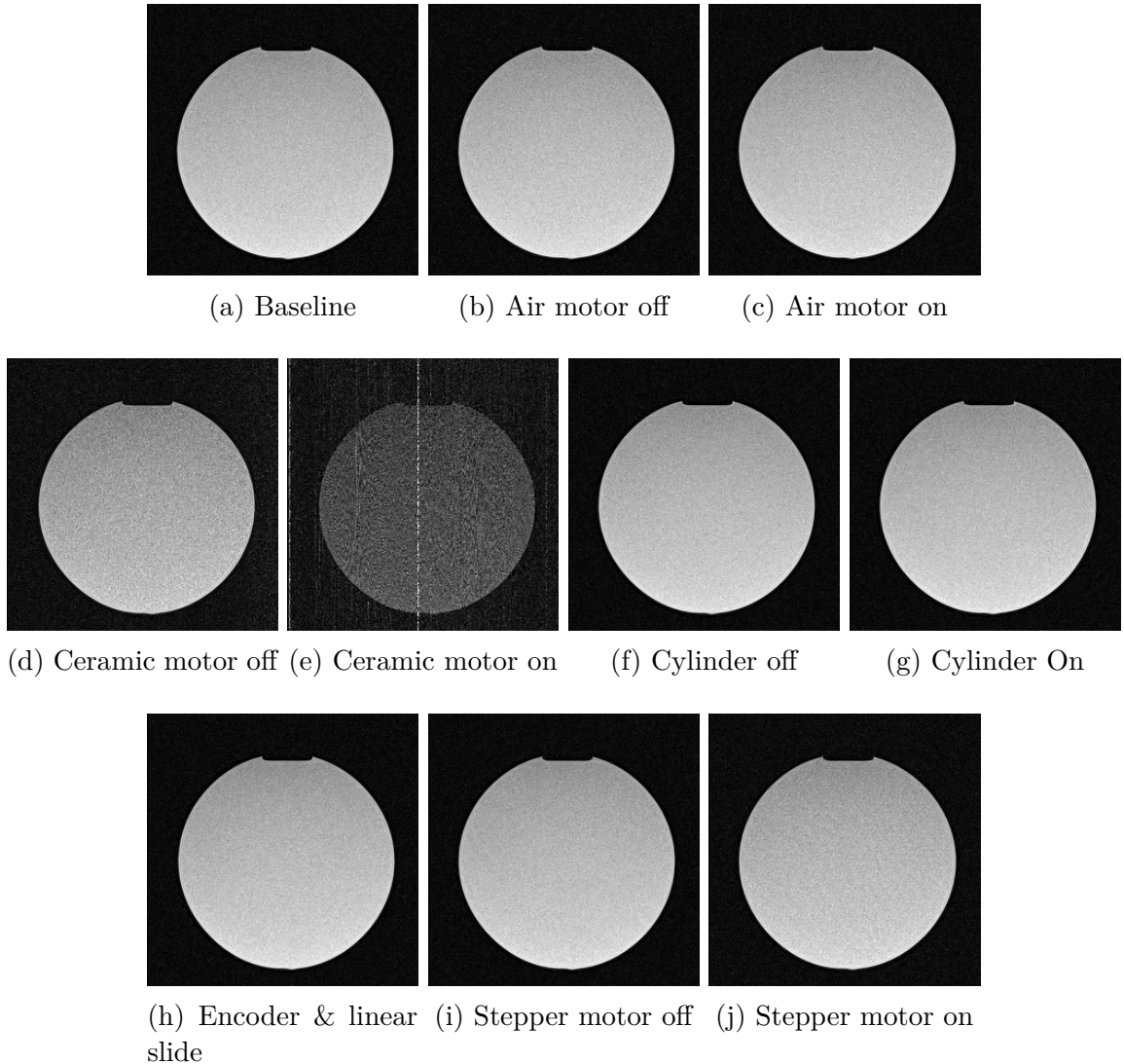


Figure 4.5: Sample scan images from the 1.5T MRI-LINAC (SE scans)

The scan images from the ceramic motor, shown in Figure 4.6, reveal some interesting insights. Without adjusting the contrast in the scan images, the RF interference artefacts when the ceramic motor is moving are immediately apparent in Figure 4.5e. Adjusting the contrast to emphasise the image artefacts (Figure 4.6), one can observe that there is random noise distributed throughout the scan image when the ceramic motor is stationary, and that there are RF interference artefacts when the ceramic motor is moving.

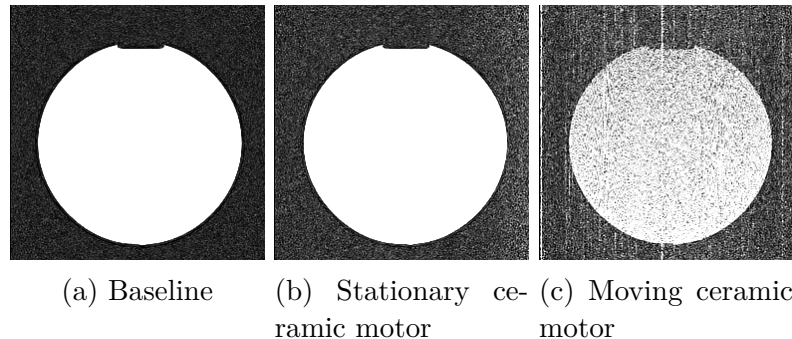


Figure 4.6: Sample scan images from the 1.5T MRI-LINAC with contrast adjusted to emphasise the image artefacts (SE scans)

The SNR results from HASTE scans at the 1.5T MRI-LINAC are shown in Figure 4.7. The results from the HASTE scan experiments also indicate that pneumatic system are more robust against SNR losses. For the ceramic motor, the drop in SNR is immediate even when stationary, and then drops even further once the motor begins moving.

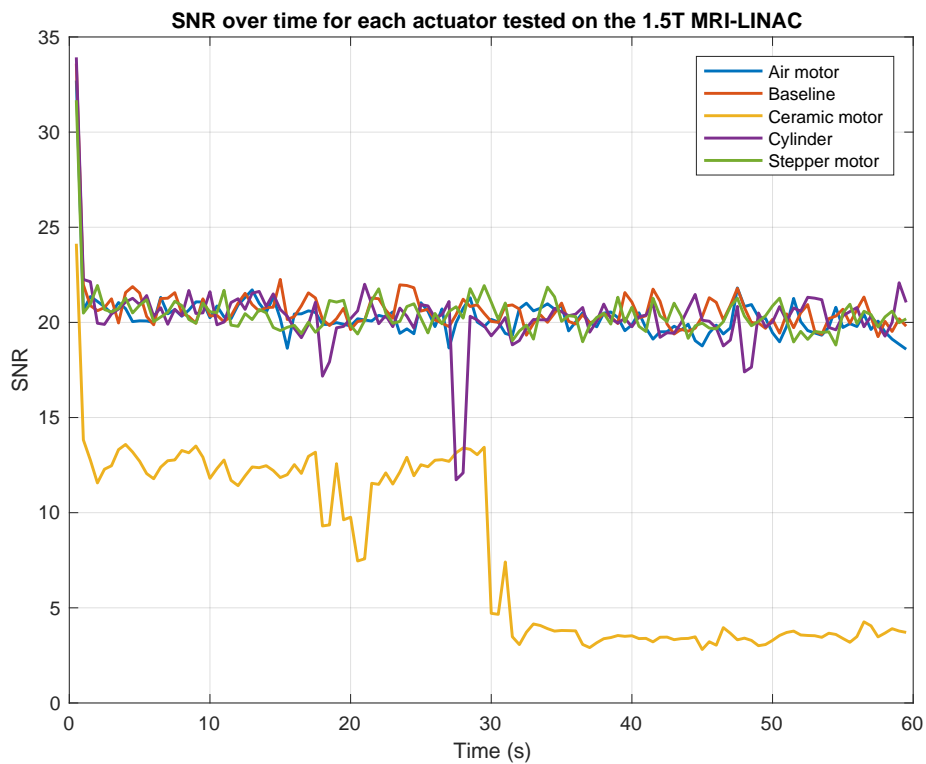


Figure 4.7: SNR results from the 1.5T MRI-LINAC (HASTE scans)

4.3 Pneumatic motor prototyping

4.3.1 Proof of concept

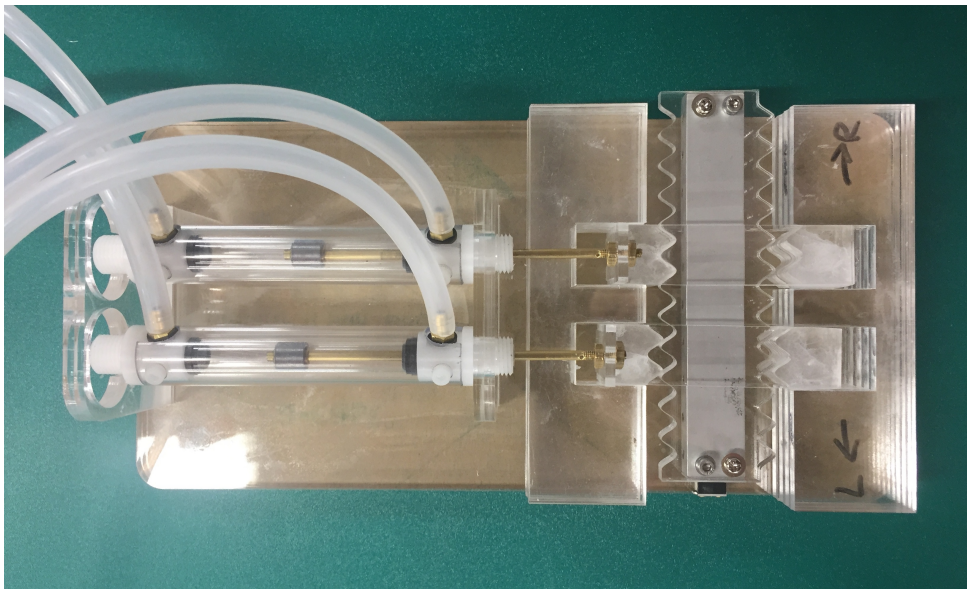


Figure 4.8: Proof of concept for stepping mechanism

The proof of concept model was fabricated as shown in Figure 4.8. The proof of concept model successfully demonstrated the stepping principle, which is illustrated in Figure 4.9. The following list details some observational notes about the proof of concept model:

- Teeth depth: if the teeth are too deep, the track struggles to move because not enough force from the pistons is being translated into lateral movement in the track.
- Teeth shape: sinusoidally shaped teeth did not wedge as easily as triangular teeth. With sinusoidal teeth, there is less surface contact – and therefore, less friction – when the pistons engage and disengage with the track.
- Air pressure: the model requires a base pressure level in the cylinders before any of the pistons move. Below the minimum pressure requirement, the model cannot overcome the frictional forces required to move the pistons and the track.

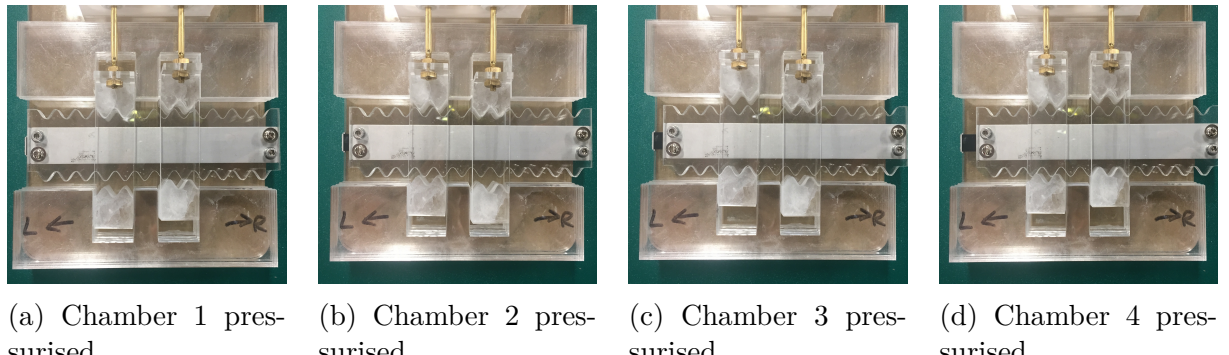


Figure 4.9: Pressurising chambers in the order 1-2-3-4 causes track to move to the right

4.3.2 Acrylic prototypes

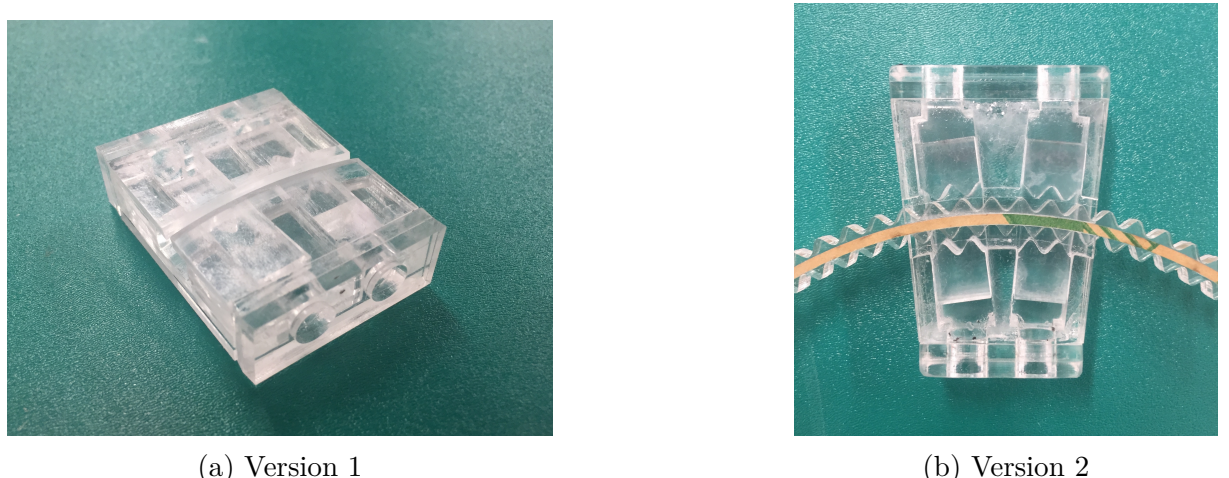


Figure 4.10: Acrylic prototypes – four chamber, curvilinear track design

Two acrylic versions of the full curvilinear prototypes were fabricated as shown in Figure 4.10. Of the two acrylic prototypes that were fabricated, only version 2 was successful. The version 1 of this four chamber, curvilinear stepper motor design had misalignments due to the inaccurate angle and separation of the chambers. These geometric issues were resolved in the second version. Some things to note about the second acrylic prototype is that there was moderate air leakage out the sides of the motor and through cracks where the acrylic parts mate together.

Resin prototypes



(a) Version 1 – four pistons



(b) Version 2 – three pistons

Figure 4.11: Resin prototypes – curvilinear track design

Two resin prototypes were fabricated as shown in Figure 4.11. Both resin models proved to be unsuccessful prototypes. For both versions, there was shrinkage in the housing which prevented the pistons from meshing properly with the track. There was also a significant amount of friction from un-sanded surfaces in the resin model.

In version 2 of the resin prototypes, the pistons proved to be too small for the tolerances that were built into the prototype. In other words, the gap between the piston and the chamber was too big relative to the size of the teeth, so that any rattling in the pistons would prevent the teeth from meshing with the track properly.

That said, choosing a different type of resin and refining the post-printing process has the potential to make the resin models a viable actuator, especially since these models have fewer mating edges where air tends to leak out of.

4.4 Actuator Characterisation

4.4.1 Load tests

Figure 4.12 shows the load capacity at varying pressure. At 1 bar pressure, the actuator did not move at all, even without the battery weights. From 1.25 bar to 3 bar, the actuator was able to achieve a stall load between 0.27N and 1.6N with a measurement error of 0.11N due to the increment size of the battery weights (11g).

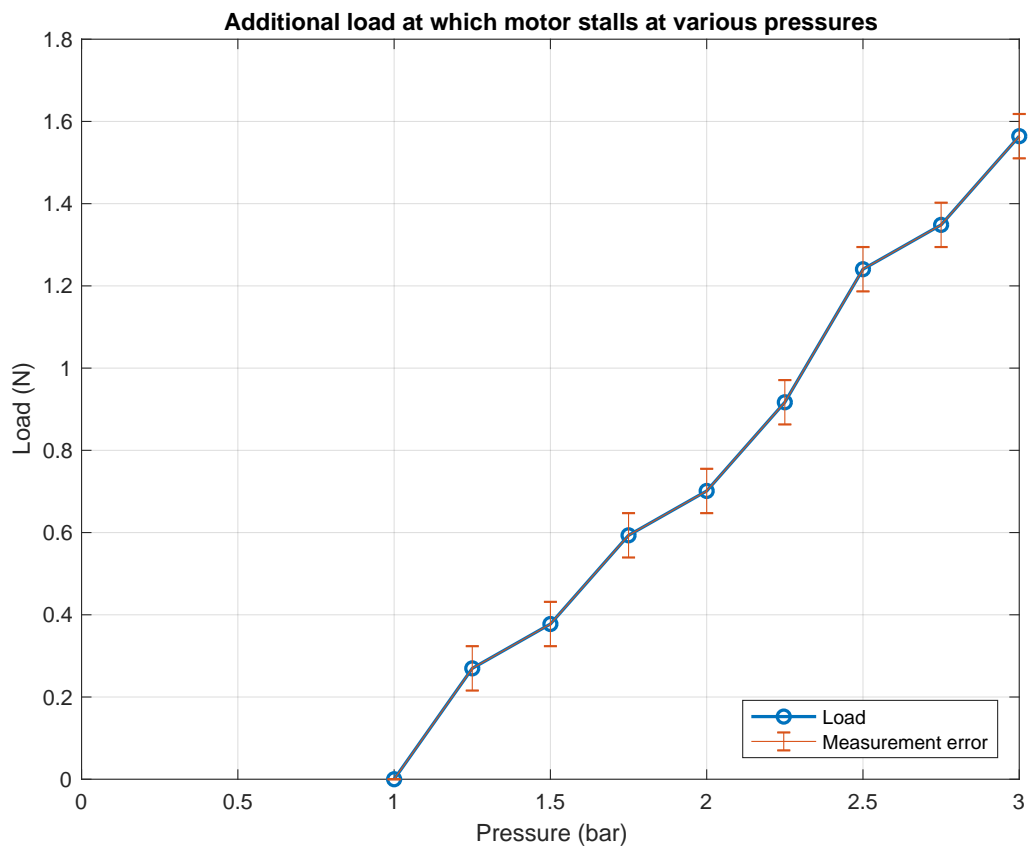


Figure 4.12: Experimental results for load capacity

4.4.2 Bandwidth tests

The experimental results for bandwidth capacity is shown in Figure 4.13. From the bandwidth tests, the maximum stepping frequency of the actuator was found to be around 37 Hz, at which the measurement error is 1.4 Hz due to the experimental increment size of the stepping duration (2ms). Experimental measurement error is at its minimum for long stepping durations (low frequencies) and at a maximum for short stepping durations (high frequencies), which is why the measurement error grows as the pressure increases and the resulting bandwidth increases.

Note, however, that the stepping frequency actually plateaus out to 37 Hz at around 2.25 bar pressure, which suggests that our pneumatic setup has an inherent bandwidth capacity that is not related to the power that the compressed air is able to deliver to the pistons.

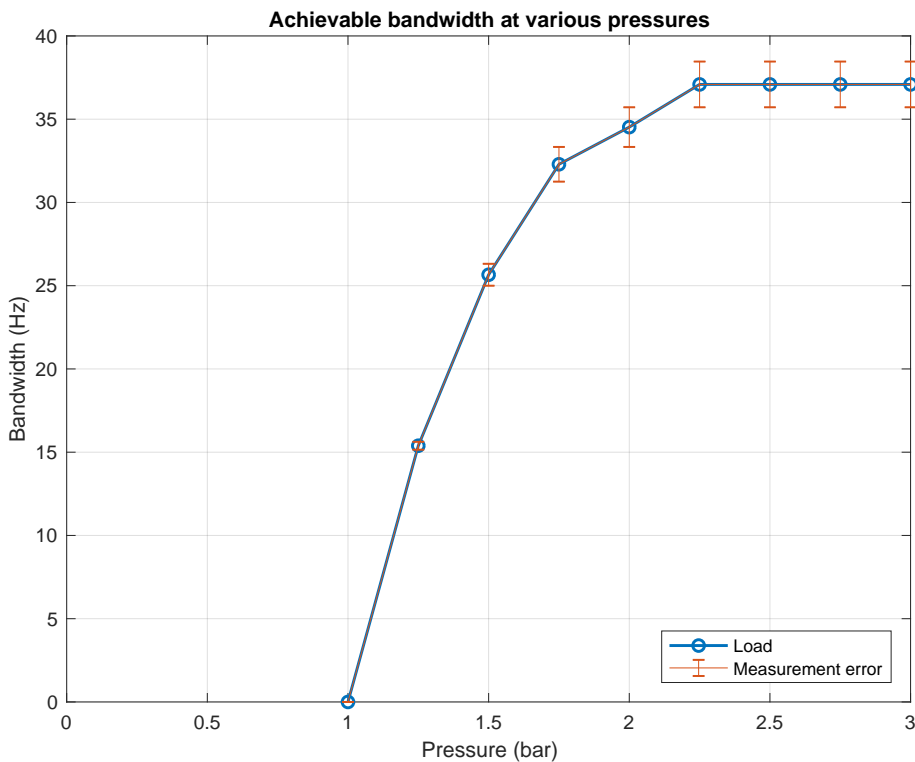


Figure 4.13: Experimental results for bandwidth capacity

Chapter 5

Discussion

In this section we discuss the results obtained from this work. Firstly, the different types of actuators tested will be evaluated in terms of practicality. Then, we analyze the SNR results, and the validity of the chosen ROIs for SNR calculation. Subsequently, we examine rooms of improvement of the proposed actuator prototype. Finally, we evaluate the bandwidth and load test results.

5.1 Preliminary actuator design

In this section, we will discuss the performance of the preliminary actuators in a qualitative manner. While all four preliminary designs were able to produce actuation, some actuators have more practicality than others. Overall, we found that all four actuators showed potential but require further development to become .

5.1.1 Ceramic motor

The ceramic motor was really compact in its open loop configuration, but quickly became bulky in its closed loop configuration. This is because the optical encoder itself is quite

bulky and had to be coupled with an intermediate rubber wheel as the transmission (Figure 3.3), making this actuation less practical than it could be in the closed loop configuration. In future, it is absolutely possible to refine this design into a more practical and slimline model as others have achieved in the academic literature [3, 14].

5.1.2 Pneumatic actuators

Rotary stepper motor

The pneumatic rotary stepper motor, on the other hand, does not require feedback control as it can operate fairly predictably in an open loop configuration. The drawback for this type of motor is that its incremental steps are far too big 90° to be useful, thus requiring an additional gearbox to scale down the step sizes.

Air motor

Similar to the ceramic motor, the air motor is another compact design that requires careful consideration for closed loop control. The difficulties of developing a close loop system for continuous pneumatic control is explained in Section 2.3.2, and is relevant to the air motor which uses continuous control of pressure to adjust its speed.

Cylinder

The pneumatic cylinder was the bulkiest of the open loop actuators because of the jig required to limit the stroke of the piston. As an actuator, the cylinder performs quite reliably because of its minimal air leakage and low friction pistons. The cylinder would not be suitable as a single axis actuator in a robotic system because it can only perform binarised movements whereas for our purposes, the robotic system will need to follow a curve or trajectory. As an example of how pneumatic cylinders can be developed into a

useful discrete actuator, Secoli et al. [18] have successfully prototyped a single-axis linear stepper motor that uses three cylinders in a binary fashion.

5.2 SNR Analysis

5.2.1 The poor MR-compatibility of ceramic motors

In all three SNR of the experiments that we performed across two MRI facilities, the ceramic motor showed the largest drops in SNR. This result is consistent with the SNR analysis results reported in the literature (see Section 2.3.1). Other researchers have investigated into this phenomenon but there is presently no general consensus on where the MR-incompatibility originates from or how best to mitigate its effects in an MRI scanner.

Aside from the effect of the low-current electrical signals that drive a ceramic motor, researchers have posited that the long wire of a ceramic motor acts as antenna to pick up external RF noise and transmit it into scan room [5, 11, 12, 39]. There is anecdotal evidence that techniques such as installing a filter panel in the scan room [31, 39] and putting the controller inside the scan room [5] can recover some SNR losses, but not all of it. There is also experimental evidence that RF shielding the ceramic motor cables minimises some of the SNR degradation [7].

While it's true that these studies indicate potential for improving the MR-compatibility of ceramic motors, we decided to pursue pneumatic designs for the second half of this thesis project. The rationale for this decision was that pneumatics already have satisfactory MR-compatibility without the need for additional systems to recover any SNR losses.

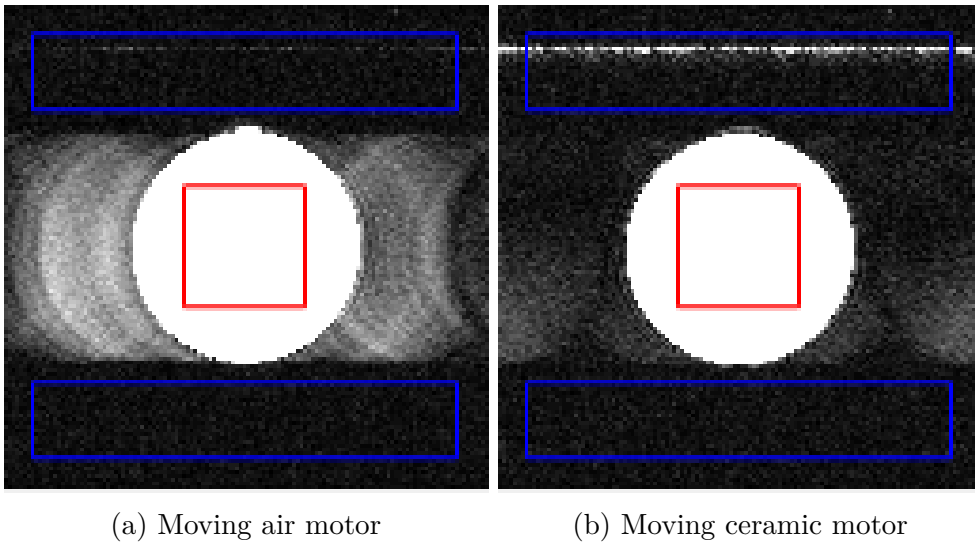


Figure 5.1: Contrast-adjusted scan image with ROI overlaid (7T small animal system) (red = signal ROI, blue = background ROI). Background ROI misses the ringing artefacts (left) but overlaps with the RF noise artefacts (right).

5.2.2 Choice of ROI

In the 7T small animal system SNR analysis results, we found that the SNR performance of the air motor was similar to pneumatic cylinder, despite the presence of ringing artefact from the vibrations of the air motor (Figure 4.3). The fact that the air motor did not experience a significant drop in SNR is due to the choice of the background ROIs. The chosen background ROIs did not overlap with the ringing artefacts, as shown in Figure 5.1, even though the ringing artefacts do contribute to noise in the scan image. At the same time, the SNR losses from the ceramic motor were very significant because the RF noise artefacts landed inside the background ROIs.

We were recommended this choice of ROIs precisely to avoid the ringing artefacts because they are present to in all the experimental data from the 7T small animal system. The ringing artefacts are almost imperceptible in all scans except for the moving air motor.

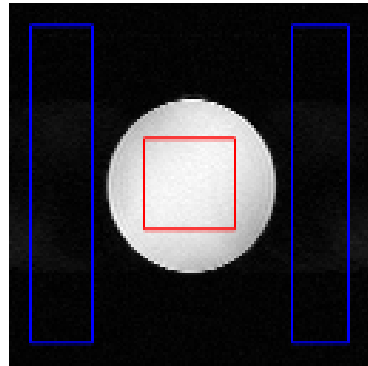


Figure 5.2: Vertical background ROIs for 7T small animal system data

If vertical background ROIs were chosen instead as in Figure 5.2, the SNR results would look significantly different as shown in Figure 5.3. The most obvious difference is that there is now a huge variability in SNR results for most of the test items, each of which was scanned three times. This extreme standard deviation range suggests that the ringing artefacts differ widely between scans of the same item. Unsurprisingly, the moving air motor demonstrated the lowest mean SNR. Even though this new choice of ROIs now takes into account the mild ringing artefacts of the air motor, the results are now meaningless because the differences in SNRs are statistically insignificant.

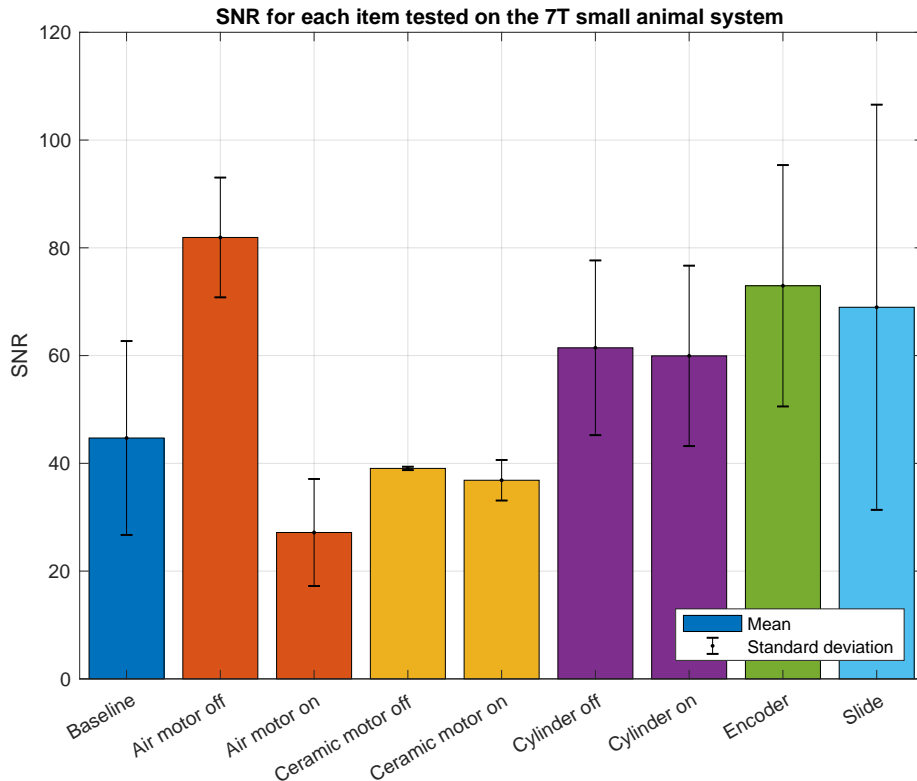


Figure 5.3: Hypothetical SNR analysis results for vertical background ROIs for the 7T small animal system data

The point here is not to over-emphasise the significance of the motion artefacts. What this discussion attempts to do is to understand the unusually good results for the moving air motor given the motion artefacts present in its scan images.

5.3 Prototyping

5.3.1 Air leakage

Air leakage in the acrylic curvilinear stepper motor was an unavoidable problem because compressed air had to escape somewhere and we had not designed an exhaust path for the air to travel. Most exhaust air travelled through the sides of the motor where there

was the largest opening, as illustrated in Figure 5.4.

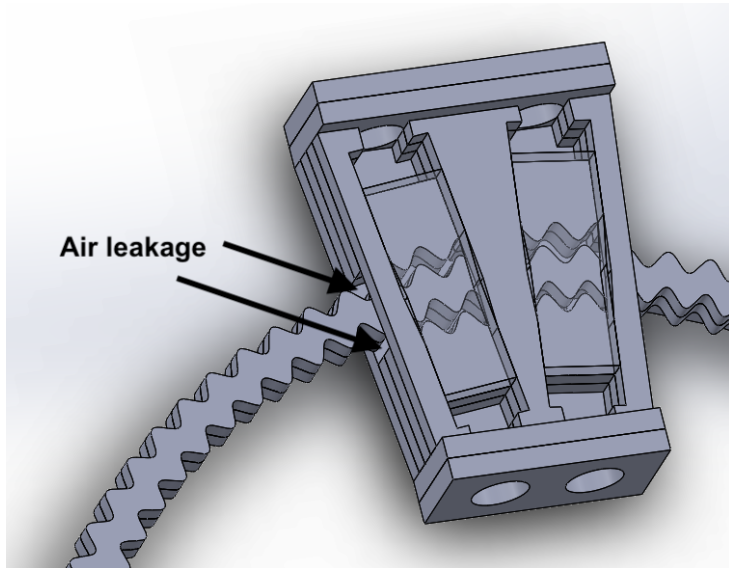


Figure 5.4: Most air leakage occurred at the sides of the acrylic curvilinear stepper motor

The problematic sources of air leakage were the cracks and crevices where the superglue did not create an airtight seal between acrylic layers. Some of these cracks were close to where the pneumatic hose delivers air to the chambers, thus reducing the efficiency of the compressed air acting on the pistons. One way we tried to mitigate this was by using Vaseline to form a seal in the chamber, but the oil was found to be too viscous and impeded the pistons' ability to move easily. Air tool oil was also used to lubricate the pistons and form a better seal in the chambers. The air tool oil ended up spraying everywhere because the fluid was so thin.

Air leakage was still present in the resin prototype, but it was less than in the acrylic prototype as the resin prototypes have a mostly resin solid body and fewer joined parts.

5.3.2 Friction and tolerancing

As the curvilinear stepper motor stepped around the circular track, we noticed that the motor would be slightly jerky at certain parts of the track because of friction that

prevented the teeth from meshing fully. If the pressure was set low enough, the motor would even stall at those parts of the track. The take-home message here is that the curvilinear stepper motor system is like a chain – it will stall at the weakest tooth. This is why for the characterisation tests we actuated the stepper motor over a wide portion of the track in both directions: so as to get a fairer measurement of the overall performance of the motor in all stages around the track.

Consequently, proper tolerancing of parts is absolutely critical in this curvilinear stepper motor design because parts that are too tight would cause the motor to stall, and parts that are too loose would allow too much compressed air to escape, thereby making the motor less efficient.

5.4 Actuator Characterisation

5.4.1 Load tests

As shown in Figure 4.12, there appears to be a roughly linear relationship between air pressure and the maximum load the curvilinear stepper motor is able to drive before it stalls. One possible reason that this may be the case is that once the motor is able to overcome a base level of frictional forces, the motor is able to translate force from the compressed air to the pistons. Note also the equation for force due to pressure applied perpendicularly to a surface is given by the equation:

$$F = PA, \quad (5.1)$$

where F is the force (N), P is the air pressure (N/m^2), and A is the area over which the pressure acts.

In the curvilinear stepper motor, compressed air acts over the same piston cross-sectional area, thus the force that is generated can be assumed to be approximately linear with

pressure.

Regarding the 1kg payload criteria for a future robotic platform from Table 1.1, we can make perform some rough calculations to examine whether the curvilinear stepper motor would be able to meet this criteria. Since each actuator has a maximum stall load of 1.6N 4.12, a 6 DOF platform would be able to drive a load up to 9.6N. The 1kg phantom itself would deliver a load of approximately 9.81N, which is close to the load capacity of a hypothetical 6 DOF platform. Keep in mind, however, that the maximum stall load (1.6N) was applied directly against the operational direction of the motor during the experiments, but in practice, the phantom load vector may be at an any angle between against and orthogonal to the direction of the motor travel.

5.4.2 Bandwidth tests

In Figure 4.13, the bandwidth of the stepper motor can be seen to increase at a decaying rate as pressure is increased. There could be a number of limiting factors that cause this plateauing out of stepping frequency:

- Tube length: the longer the pneumatic tubes, the harder it is to switch pressures at a higher frequency. This is because air is highly compressible and has a long transport delay as it travels through the tube, therefore causing a low-pass filtering effect on the switching pressure levels.
- Mechanical inefficiencies: there may be a limit to the speed at which the pistons are able to mesh and unmesh with the toothed track due to the friction profile of the sliding surfaces.

With reference back to our original frequency requirement of 3.3 Hz trajectory sampling Table 1.1, the maximum stepping frequency (37 Hz) of the stepper motor can accomodate for the trajectory sampling frequency by more than tenfold.

Chapter 6

Conclusions

6.1 Summary

In this thesis project, we have conducted research into MR-compatible actuation methods for benchmarking MR-guided radiotherapy. As part of our investigation into appropriate actuation methods, we have implemented a ceramic motor, pneumatic rotary motor, air motor, and pneumatic cylinder, and have compared and contrasted their qualities. To verify these actuators' MR-compatibility, we conducted experiments on a 7T small animal system and on the 1.5T MRI-LINAC to determine the impact that the actuators have on scan image SNR. Based on the SNR analysis results of our experiments, we decided to pursue a pneumatic actuator design and developed a curvilinear stepper motor. We then performed a series of tests on the stepper motor to assess whether this type of motor would be suitable for a robotic platform application as a benchmarking tool in MR-guided radiotherapy.

6.2 Findings and contributions

From our investigation into MR-compatible actuation methods, we can conclude that pneumatic actuation methods have minimal impact on MR-image quality, whereas ceramic motors exhibit a moderate to severe impact on MR-image. Our SNR analysis results are consistent with the academic literature, thereby validating the work of previous authors who have published similar findings [7, 12–14]. Another important finding from our work is that the curvilinear stepper motor design is capable of up to 1.6N stall load and 37 Hz maximum stepping frequency. From this result and our discussion of it in Section 5.4, we can conclude there is potential for this prototype to be refined and scaled up into a robotic platform that meets the specifications in Table 1.1.

6.3 Future work

There is plenty of scope for future work to expand on the results from this thesis project. The following presents some recommendations on how to extend that work that was achieved in this thesis project.

6.3.1 Refining the pneumatic curvilinear stepper motor

Based on the encouraging results from our load and torque tests in Section 4.4, we would recommend that a good place to start with future work is to refine the curvilinear stepper motor and improve its performance further. As discussed in Section 5.3, unwanted air leakage and dimensional tolerancing are the two main problems that need to be addressed in future designs.

6.3.2 Simulation of a pneumatic Stewart platform

Figure 6.1 is a depiction of a novel Stewart platform design that we drew by hand, and definitely not on Solidworks. There are six pneumatic curvilinear stepper motors that can move freely around a circular track like carriages. The struts are ball-jointed on both ends so that the platform may translate and rotate into many different positions and orientations, depending on the configuration of the stepper motor carriages.

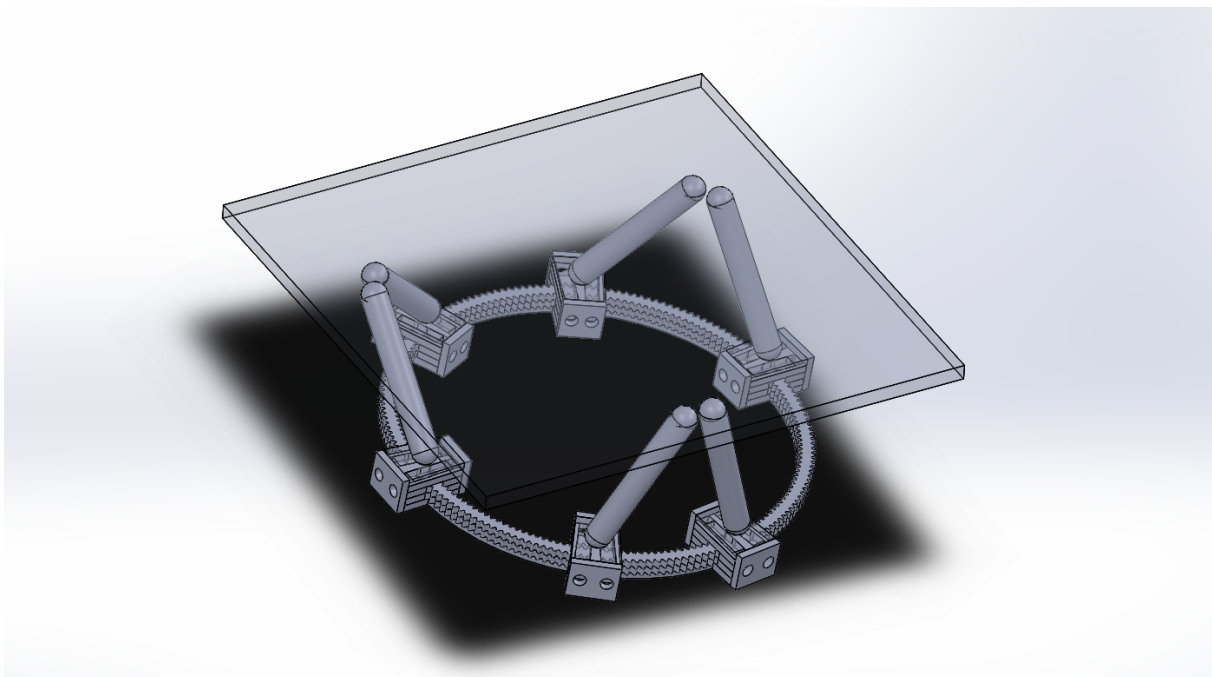


Figure 6.1: 6-DOF Stewart platform with pneumatic curvilinear stepper motors as carriages

Stewart platforms have very complicated geometries and have singularities in its workspace, like any robotic system. In a future pneumatic Stewart platform, there would also be the added complexity of the discretised step sizes of the pneumatic stepper motors. Thus, it would be a worthwhile exercise to simulate the kinematics of a pneumatic Stewart platform because it is still unknown how a stepper motor would behave in this type of robotic platform.

Bibliography

- [1] P. J. Keall, M. Barton, S. Crozier *et al.*, “The australian magnetic resonance imaging–linac program,” in *Seminars in radiation oncology*, vol. 24, no. 3. Elsevier, 2014, pp. 203–206.
- [2] N. Maughan, D. Muccigrosso, H. Schultejans, R. Bera, and P. Parikh, “Continuous tracking of lung tumor motion at 3.3 hz or faster is necessary to accurately represent motion,” *International Journal of Radiation Oncology? Biology? Physics*, vol. 96, no. 2, p. E679, 2016.
- [3] N. V. Tsekos, A. Khanicheh, E. Christoforou, and C. Mavroidis, “Magnetic resonance–compatible robotic and mechatronics systems for image-guided interventions and rehabilitation: a review study,” *Annu. Rev. Biomed. Eng.*, vol. 9, pp. 351–387, 2007.
- [4] A. Berger, “How does it work?: Magnetic resonance imaging,” *BMJ: British Medical Journal*, vol. 324, no. 7328, p. 35, 2002.
- [5] R. Gassert, A. Yamamoto, D. Chapuis, L. Dovat, H. Bleuler, and E. Burdet, “Actuation methods for applications in mr environments,” *Concepts in Magnetic Resonance Part B: Magnetic Resonance Engineering: An Educational Journal*, vol. 29, no. 4, pp. 191–209, 2006.
- [6] D. Stoianovici, A. Patriciu, D. Petrisor, D. Mazilu, and L. Kavoussi, “A new type of motor: pneumatic step motor,” *IEEE/ASME Transactions On Mechatronics*, vol. 12, no. 1, pp. 98–106, 2007.
- [7] A. Krieger, I. Iordachita, S.-E. Song, N. B. Cho, P. Guion, G. Fichtinger, and L. L. Whitcomb, “Development and preliminary evaluation of an actuated mri-compatible robotic device for mri-guided prostate intervention,” in *Robotics and Automation (ICRA), 2010 IEEE International Conference on*. IEEE, 2010, pp. 1066–1073.
- [8] Z. Guo, Z. Dong, K.-H. Lee, C. L. Cheung, H.-C. Fu, J. D. Ho, H. He, W.-S. Poon, D. T.-M. Chan, and K.-W. Kwok, “Compact design of a hydraulic driving robot for intra-operative mri-guided bilateral stereotactic neurosurgery,” *IEEE Robotics and Automation Letters*, vol. 3, no. 3, pp. 2515–2522, 2018.

- [9] G. R. Sutherland, I. Latour, A. D. Greer, T. Fielding, G. Feil, and P. Newhook, “An image-guided magnetic resonance-compatible surgical robot,” *Neurosurgery*, vol. 62, no. 2, pp. 286–293, 2008.
- [10] K. Chinzei, N. Hata, F. A. Jolesz, and R. Kikinis, “Mr compatible surgical assist robot: System integration and preliminary feasibility study,” in *International Conference on Medical Image Computing and Computer-Assisted Intervention*. Springer, 2000, pp. 921–930.
- [11] K. Chinzei, R. Kikinis, and F. A. Jolesz, “Mr compatibility of mechatronic devices: design criteria,” in *International Conference on Medical Image Computing and Computer-Assisted Intervention*. Springer, 1999, pp. 1020–1030.
- [12] G. S. Fischer, A. Krieger, I. Iordachita, C. Csoma, L. L. Whitcomb, and G. Fichtinger, “Mri compatibility of robot actuation techniques—a comparative study,” in *International Conference on Medical Image Computing and Computer-Assisted Intervention*. Springer, 2008, pp. 509–517.
- [13] N. V. Tsekos, A. Özcan, and E. Christoforou, “A prototype manipulator for magnetic resonance-guided interventions inside standard cylindrical magnetic resonance imaging scanners,” *Journal of biomechanical engineering*, vol. 127, no. 6, pp. 972–980, 2005.
- [14] H. Su, M. Zervas, G. A. Cole, C. Furlong, and G. S. Fischer, “Real-time mri-guided needle placement robot with integrated fiber optic force sensing,” in *Robotics and Automation (ICRA), 2011 IEEE International Conference on*. IEEE, 2011, pp. 1583–1588.
- [15] E. Hempel, H. Fischer, L. Gumb, T. Höhn, H. Krause, U. Voges, H. Breitwieser, B. Gutmann, J. Durke, M. Bock *et al.*, “An mri-compatible surgical robot for precise radiological interventions,” *Computer Aided Surgery*, vol. 8, no. 4, pp. 180–191, 2003.
- [16] K. Masamune, E. Kobayashi, Y. Masutani, M. Suzuki, T. Dohi, H. Iseki, and K. Takakura, “Development of an mri-compatible needle insertion manipulator for stereotactic neurosurgery,” *Journal of Image Guided Surgery: Official Journal of the International Society for Computer Aided Surgery (ISCAS)*, vol. 1, no. 4, pp. 242–248, 1995.
- [17] B. Yang, U. X. Tan, A. B. McMillan, R. Gullapalli, and J. P. Desai, “Design and control of a 1-DOF MRI-compatible pneumatically actuated robot with long transmission lines,” *IEEE/ASME Transactions on Mechatronics*, 2011.
- [18] R. Secoli, M. Robinson, M. Brugnoli, and F. Rodriguez y Baena, “A low-cost, high-field-strength magnetic resonance imaging-compatible actuator,” *Proceedings of the Institution of Mechanical Engineers, Part H: Journal of Engineering in Medicine*, vol. 229, no. 3, pp. 215–224, 2015.

- [19] A. Wineland, Y. Chen, and Z. T. H. Tse, “Magnetic resonance imaging compatible pneumatic stepper motor with geneva drive,” *Journal of Medical Devices*, vol. 10, no. 2, p. 020950, 2016.
- [20] J. A. Cunha, I.-C. Hsu, J. Pouliot, M. Roach III, K. Shinohara, J. Kurhanewicz, G. Reed, and D. Stoianovici, “Toward adaptive stereotactic robotic brachytherapy for prostate cancer: demonstration of an adaptive workflow incorporating inverse planning and an mr stealth robot,” *Minimally Invasive Therapy & Allied Technologies*, vol. 19, no. 4, pp. 189–202, 2010.
- [21] Y. Chen, C. D. Mershon, and Z. T. H. Tse, “A 10-mm mr-conditional unidirectional pneumatic stepper motor,” *IEEE/ASME Transactions on Mechatronics*, vol. 20, no. 2, pp. 782–788, 2015.
- [22] B. T. Larson, A. G. Erdman, N. V. Tsekos, E. Yacoub, P. V. Tsekos, and I. G. Koutlas, “Design of an mri-compatible robotic stereotactic device for minimally invasive interventions in the breast,” *Journal of Biomechanical Engineering*, vol. 126, no. 4, pp. 458–465, 2004.
- [23] B. Yang, S. Roys, U.-X. Tan, M. Philip, H. Richard, R. P. Gullapalli, and J. P. Desai, “Design, development, and evaluation of a master–slave surgical system for breast biopsy under continuous mri,” *The International journal of robotics research*, vol. 33, no. 4, pp. 616–630, 2014.
- [24] M. A. Tavallaei, P. M. Johnson, J. Liu, and M. Drangova, “Design and evaluation of an mri-compatible linear motion stage,” *Medical physics*, vol. 43, no. 1, pp. 62–71, 2016.
- [25] M. K. Stam, S. P. Crijns, B. A. Zonnenberg, M. M. Barendrecht, M. van Vulpen, J. J. Lagendijk, and B. W. Raaymakers, “Navigators for motion detection during real-time mri-guided radiotherapy,” *Physics in Medicine & Biology*, vol. 57, no. 21, p. 6797, 2012.
- [26] V. Groenhuis, F. J. Siepel, J. Veltman, and S. Stramigioli, “Design and characterization of stormram 4: an mri-compatible robotic system for breast biopsy,” in *Intelligent Robots and Systems (IROS), 2017 IEEE/RSJ International Conference on*. IEEE, 2017, pp. 928–933.
- [27] A. Krieger, R. C. Susil, G. Fichtinger, E. Atalar, and L. L. Whitcomb, “Design of a novel mri compatible manipulator for image guided prostate intervention,” in *Robotics and Automation, 2004. Proceedings. ICRA ’04. 2004 IEEE International Conference on*, vol. 1. IEEE, 2004, pp. 377–382.
- [28] D. Stoianovici, D. Song, D. Petrisor, D. Ursu, D. Mazilu, M. Mutener, M. Schar, and A. Patriciu, ““mri stealth” robot for prostate interventions,” *Minimally Invasive Therapy & Allied Technologies*, vol. 16, no. 4, pp. 241–248, 2007.

- [29] R. C. Susil, K. Camphausen, P. Choyke, E. R. McVeigh, G. S. Gustafson, H. Ning, R. W. Miller, E. Atalar, C. N. Coleman, and C. Ménard, “System for prostate brachytherapy and biopsy in a standard 1.5 t mri scanner,” *Magnetic Resonance in Medicine: An Official Journal of the International Society for Magnetic Resonance in Medicine*, vol. 52, no. 3, pp. 683–687, 2004.
- [30] S. DiMaio, S. Pieper, K. Chinzei, N. Hata, S. Haker, D. Kacher, G. Fichtinger, C. Tempany, and R. Kikinis, “Robot-assisted needle placement in open mri: system architecture, integration and validation,” *Computer Aided Surgery*, vol. 12, no. 1, pp. 15–24, 2007.
- [31] G. R. Sutherland, I. Latour, and A. D. Greer, “Integrating an image-guided robot with intraoperative mri,” *IEEE engineering in medicine and biology magazine*, vol. 27, no. 3, pp. 59–65, 2008.
- [32] A. Patriciu, D. Petrisor, M. Muntener, D. Mazilu, M. Schar, and D. Stoianovici, “Automatic brachytherapy seed placement under mri guidance,” *IEEE Transactions on Biomedical Engineering*, vol. 54, no. 8, pp. 1499–1506, 2007.
- [33] N. V. Tsekos, E. Christoforou, and A. ÖZCAN, “A general-purpose mr-compatible robotic system: implementation and image guidance for performing minimally invasive interventions,” *IEEE engineering in medicine and biology magazine: the quarterly magazine of the Engineering in Medicine & Biology Society*, vol. 27, no. 3, p. 51, 2008.
- [34] G. S. Fischer, I. Iordachita, C. Csoma, J. Tokuda, S. P. DiMaio, C. M. Tempany, N. Hata, and G. Fichtinger, “Mri-compatible pneumatic robot for transperineal prostate needle placement,” *IEEE/ASME transactions on mechatronics*, vol. 13, no. 3, pp. 295–305, 2008.
- [35] *User Manual HR Motors*, Nanomotion, LTD, 1 2015, rev B.
- [36] V. Groenhuis, “Pneumatic stepper motor: Bourke engine,” <https://www.thingiverse.com/thing:2813533>, March 2018.
- [37] M. Firbank, A. Coulthard, R. Harrison, and E. Williams, “A comparison of two methods for measuring the signal to noise ratio on mr images,” *Physics in Medicine & Biology*, vol. 44, no. 12, p. N261, 1999.
- [38] U. U. Circular-Base-Stewart-Platform). Circular-base-stewart-platform, part 10, the motion-demo. Youtube. [Online]. Available: <https://www.youtube.com/watch?v=RR4pmNEWuo4>
- [39] G. Cole, J. Pilitsis, and G. S. Fischer, “Design of a robotic system for mri-guided deep brain stimulation electrode placement,” in *Robotics and Automation, 2009. ICRA '09. IEEE International Conference on*. IEEE, 2009, pp. 4450–4456.

Appendix: save trees, save money

All our source code, CAD models, and raw scan data can be found on this GitHub repository:

<https://github.com/xueyinz/mr-compatible-actuators>

Videos of the actuators in motion can be found in this YouTube playlist:

<https://www.youtube.com/playlist?list=PLU-MIqwHqpJv1jt9WpnXpGETKMDiAD818>